

Gut microbiota-dependent increase in phenylacetic acid induces endothelial cell senescence during aging

Received: 15 November 2023

Accepted: 2 April 2025

Published online: 12 May 2025

 Check for updates

Seyed Soheil Saeedi Saravi ^{1,2,20} , Benoit Pugin³, Florentin Constancias³, Khatereh Shabanian^{1,2}, Marianne Spalinger⁴, Aurélien Thomas ^{5,6}, Sylvain Le Gludic^{5,6}, Taraneh Shabanian^{1,2}, Gergely Karsai ⁷, Manuel Colucci ^{8,9}, Cristina Menni ^{10,11,12}, Ilias Attaye^{10,13}, Xinyuan Zhang ¹⁰, Meret Sarah Allemann ^{14,15}, Pratintip Lee^{14,15}, Alessia Visconti^{10,16}, Mario Falchi ¹⁰, Andrea Alimonti ^{8,9,17,18,19}, Frank Ruschitzka^{1,2}, Francesco Paneni^{1,2} & Jürg H. Beer ^{14,15,20} 

Endothelial cell senescence is a key driver of cardiovascular aging, yet little is known about the mechanisms by which it is induced in vivo. Here we show that the gut bacterial metabolite phenylacetic acid (PAA) and its byproduct, phenylacetylglutamine (PAGln), are elevated in aged humans and mice. Metagenomic analyses reveal an age-related increase in PAA-producing microbial pathways, positively linked to the bacterium *Clostridium* sp. ASF356 (*Clos*). We demonstrate that colonization of young mice with *Clos* increases blood PAA levels and induces endothelial senescence and angiogenic incompetence. Mechanistically, we find that PAA triggers senescence through mitochondrial H₂O₂ production, exacerbating the senescence-associated secretory phenotype. By contrast, we demonstrate that fecal acetate levels are reduced with age, compromising its function as a Sirt1-dependent senomorphic, regulating proinflammatory secretion and redox homeostasis. These findings define PAA as a mediator of gut–vascular crosstalk in aging and identify sodium acetate as a potential microbiome-based senotherapy to promote healthy aging.

Aging is a substantial risk factor for prevalent cardiovascular diseases (CVDs), affecting millions of people worldwide¹. The alarming rise in CVD incidence in older adults emphasizes our inadequate understanding of its development with age². Dysfunctional endothelial cells (ECs) are increasingly recognized to contribute to CVDs³. Advanced age causes cellular senescence in ECs, a crucial factor in EC dysfunction in older adults⁴. Senescent ECs (SECs) undergo a variety of persistent alterations, including epigenetic modifications, irreversible cell-cycle arrest, DNA instability and the senescence-associated secretory phenotype (SASP), which impairs angiogenic capacity and vascular function⁵. Therefore, accumulation of SECs is considered a primary driver to aging-related CVDs.

Oxidative stress is one identified trigger of stress-induced senescence in ECs⁶. Converging evidence suggests that gut microbiota, a yet underappreciated endocrine organ, regulates oxidative-regulated host genes involved in endothelial biology⁷. Although such studies have linked gut microbiota with CVD⁸, there is limited evidence on its role in EC senescence and the molecular mechanisms in aging organisms.

With advanced age, alterations of specific gut-derived metabolites such as aromatic amino acid derivatives might contribute to CVD through prolonged oxidative stress and inflammation⁹. One such example is phenylacetic acid (PAA) and its derivative phenylacetylglutamine (PAGln), which are produced from phenylalanine by commensal

A full list of affiliations appears at the end of the paper.  e-mail: soheil.saeedi@uzh.ch; hansjuerg.beer@ksb.ch

microbial *porA* or *ppf* genes¹⁰. These metabolites are positively associated with cardiovascular and all-cause mortality in patients with chronic kidney disease (CKD)¹¹ and heart failure¹². In preclinical models, PAA stimulated reactive oxygen species (ROS) production and further inflammation in ECs¹³, explaining its role in vascular damage in CKD. Similarly, PAA-derived PAGIn fostered ROS production and apoptosis in cardiomyocytes, compromising their contractility¹². In this study, we observed higher plasma concentrations of PAA and PAGIn in both the TwinsUK human aging cohort and aged mice, hypothesizing that elevated levels of these two metabolites during aging may actively promote EC senescence and vascular dysfunction. We aimed to uncover mechanisms linking aging gut-derived PAA with EC senescence and dysfunction and to explore microbiome-based therapeutic strategies for senescence rescue and restoring angiogenic capacity in these cells.

Beyond the metabolites, gut microbiota produces a myriad of other metabolites like short-chain fatty acids (SCFAs), mainly including acetate, propionate and butyrate, which circumvent atherosclerosis and other CVD risk factors⁹. It is well characterized that >70% of colonic acetate, but only small amounts of propionate and butyrate, reach circulation after hepatic metabolism¹⁴. We have previously reported that aging markedly reduces fecal acetate levels by up to 80% due to the depletion of acetate-producing bacteria, such as *Prevotella* and *Rikenellaceae_RC9_gut_group*¹⁵. Notably, the depletion of these bacteria in the microbiome has been ubiquitously observed in CVD and is associated with disease severity¹⁶. Converting acetate to acetyl-CoA in mitochondria, quiescent ECs can sustain the tricarboxylic acid (TCA) cycle and redox homeostasis, protecting themselves against oxidative stress¹⁷. Acetate also controls epigenetic alterations by regulating histone acetylation/deacetylation critical to EC phenotype and function¹⁷. Accordingly, we hypothesized that exogenous acetate might mitigate PAA-induced oxidative stress and associated epigenetic alterations driving EC senescence, offering therapeutic potential for EC dysfunction in aging. Notably, our findings suggest acetate may help ECs escape senescence and protect against age-related arterial dysfunction and associated CVD.

Results

Gut microbiota link to elevated PAA and PAGIn in aging

Our data identified markedly higher plasma concentrations of PAA and PAGIn in aged mice (>24 months) compared to young mice (>3 months), as detected by targeted metabolomics (Fig. 1a–c). To rule out kidney function effects on age-related increases in plasma levels of PAA and PAGIn, mice were matched for sex, body weight and renal function (Supplementary Fig. 1a–c). Similar trends were observed in data from the TwinsUK human cohort (<https://twinsuk.ac.uk/>), where non-targeted metabolomics confirmed age-associated increases in PAA and PAGIn (Fig. 1d). Accordingly, linear regression analysis between metabolite concentrations and age revealed that both metabolites

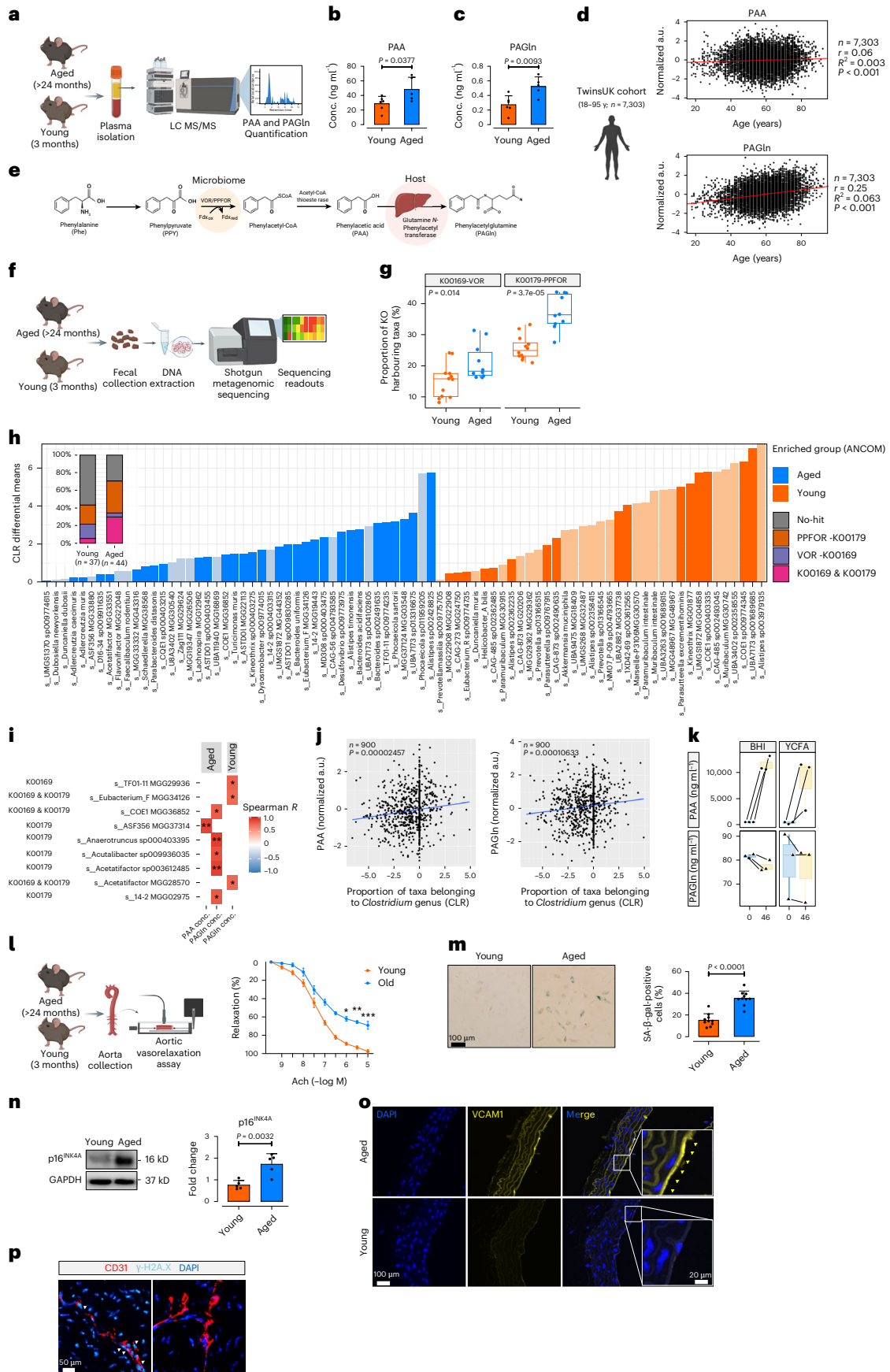
were age-dependently elevated in 7,303 individuals between 18–95 years old (PAA, $r = 0.06$, $R^2 = 0.003$, $P < 0.001$; PAGIn, $r = 0.25$, $R^2 = 0.063$, $P < 0.001$).

Previous studies have shown that gut microbiota convert dietary phenylalanine into PAA via a metaorganismal pathway, at which point host PAA-to-glutamine conjugation leads to PAGIn generation¹⁰. Our supplementary and others^{10,18} studies revealed that antibiotic suppression of gut microbiota markedly reduces circulating PAA and PAGIn levels, reinforcing gut microbial involvement (Supplementary Fig. 2a,b). Two distinct microbial pathways (phenylpyruvate:ferredoxin oxidoreductase (PPFOR) and α -ketoisovalerate:ferredoxin oxidoreductase (VOR)) contribute to PAA biosynthesis via oxidative decarboxylation of phenylalanine¹⁰ (Fig. 1e). To investigate whether the pathways dominate in aging, we performed fecal shotgun metagenomics within our mouse model of chronological aging (Fig. 1f). At the initial step, our data unsurprisingly revealed significant alterations in both α -diversity (richness and evenness) and β -diversity indices (Extended Data Fig. 1a,b) in the gut microbiome of aged mice. The Kyoto Encyclopedia of Genes and Genomes (KEGG) analysis identified a significantly higher abundance of *ppfor* and *vor* gene homologs in the microbiome of aged mice ($P = 3.7 \times 10^{-5}$ for *ppfor*; $P = 0.014$ for *vor*; Fig. 1g). A significant correlation between plasma PAA levels and percentage of either *ppfor*- or *vor*-positive genomes was also observed in the aged microbiomes ($R^2 = 0.52$ for *ppfor* and $R^2 = 0.47$ for *vor*, $P < 0.0001$; Extended Data Fig. 1d); however, plasma PAGIn concentrations displayed weaker associations with *ppfor*- or *vor*-harboring bacteria in aged mice ($R^2 = 0.24$ for *ppfor*; $R^2 = 0.085$ for *vor*; Extended Data Fig. 1d). In line with the above findings, the centered log ratio (CLR) by analysis of composition of microbiomes (ANCOM) demonstrates differentially abundant bacterial taxa harboring VOR, PPFOR or both homologs in the aged microbiomes. Accordingly, a -1.7-fold higher proportion of PPFOR or VOR + PPFOR homologs was enriched in aged mice compared to those in young mice (72% versus 42%; Fig. 1h). Focusing on specific bacteria linked to age-related PAA elevation, Spearman's rank correlation analysis pinpointed *Clostridium* sp. ASF356 MGG37314 as the only PPFOR-positive bacterium positively associated with plasma PAA levels in aged mice (Fig. 1i). This bacterium was moderately abundant in aged microbiomes (ranging from 0.012099% to 1.400074%; Extended Data Fig. 1e). Five other taxa from the class *Clostridia* displayed a positive association with plasma PAGIn, but not PAA, in aged mice. To translate our observations to humans, we conducted a taxonomic profiling in individuals enrolled in the TwinsUK study ($n = 900$). Our findings revealed a substantial enrichment of bacterial taxa belonging to the *Clostridium* genus (harboring *ppfor* gene) in older individuals, correlating more strongly with PAA ($P = 0.00002457$) than PAGIn ($P = 0.00010633$) (Fig. 1j). To further validate the functional role of *Clostridium* sp. ASF356 MGG37314 in PAA formation, we cultivated an axenic culture and tested for PAA production in phenylalanine-containing brain heart infusion or yeast

Fig. 1 | Reflection of age in plasma levels of gut microbiota-derived metabolites PAA and PAGIn. a, Schematic of quantification of plasma PAA and PAGIn in young (3-month-old) and aged (>24-month-old) C57BL/6J male and female mice.

b, c, Plasma PAA (**b**) and PAGIn (**c**) levels were measured by LC-MS/MS in mice ($n = 6$). **d**, Correlation between plasma PAA (left) and PAGIn (right) concentrations and chronological age in the TwinsUK cohort ($n = 7,303$, male and female). **e**, Schema for PAA production from dietary phenylalanine (Phe) via the bacterial VOR/PPFOR system. **f**, Shotgun metagenomics workflow for analyzing mouse fecal microbiomes. **g**, Distribution of VOR and PPFOR gene homologs (%) in microbiomes of aged and young mice ($n = 5-6$). KOO169, VOR; KOO179, PPFOR. **h**, Bar plot depicting age-associated abundance of fecal microbiota profiles at strain level (dark colors represent taxa harboring VOR or PPFOR homologs). The leftmost bar plot demonstrates the proportion of VOR, PPFOR or VOR + PPFOR detected in taxa enriched in aged ($n = 44$) versus young ($n = 37$) mice. **i**, Heatmap shows correlations between plasma PAA or PAGIn levels and gut bacteria among the top enriched taxa in aged versus young mice ($n = 5-6$). **j**, Correlation between plasma PAA (left) and PAGIn (right) concentrations and

abundance (%) of *Clostridium* taxa in human participants ($n = 900$, TwinsUK; male and female). **k**, PAA (top) and PAGIn (below) concentrations in the supernatants of anaerobic cultures from *Clostridium* sp. ASF356 ($n = 8$). **l**, Schematic of ex vivo force tension myography. Aortic rings exhibit vasorelaxation responses (%) to acetylcholine (ACh) ($n = 10$). **m**, SA- β -gal staining of ECs from the ascending aortas of mice ($n = 5-6$) and quantification of SA- β -gal⁺ cells (%). **n, o**, Immunoblots and immunofluorescence represent the expression of p16^{INK4a} (**n**) and VCAM1 (**o**) in aortic ECs ($n = 5-6$). **p**, γ -H2A.X immunostaining in CD31⁺ ECs ($n = 5-6$). Scale bars, 20, 50 and 100 μ m. Error bars represent s.d. (**b, c, m, n**) or s.e.m. (**g, k, l**) or 95% confidence intervals (**d**). Statistical analysis was performed using a two-tailed unpaired Student's *t*-test (**b, c, l-n**), two-tailed Pearson correlation analysis (**d**), two-tailed Mann-Whitney *U*-test (**g, k**), ANCOM method for microbial abundance analysis (**h**), two-sided Spearman's rank correlation test (**i**) and linear mixed model CLR transformation (**j**). Data are shown as median with min-max; boxes represent interquartile range (IQR); center lines represent the median; whiskers extend from the min to max values (**g, k**). Images created with BioRender.com (**a, d-f, i**). * $P < 0.05$, ** $P < 0.01$, *** $P < 0.001$.



casitone fatty acids medium under anaerobic condition by liquid chromatography tandem mass spectrometry (LC-MS/MS) (Fig. 1k). These results suggest that *Clostridium* sp. ASF356 commensal in the aged microbiome contributes to higher circulating PAA levels.

Aged mice exhibited marked endothelial dysfunction, evidenced by reduced endothelium-dependent relaxation to acetylcholine. As shown in Fig. 1l, maximal relaxation at 10^{-5} M acetylcholine was significantly lower in aged mice ($97.57 \pm 1.91\%$ in young versus $69.13 \pm 4.25\%$ in aged; $P < 0.001$) with a rightward dose-response shift (half maximal effective concentration (EC_{50}) 34.23 ± 9.01 nM in young versus 51.33 ± 12.32 nM in aged; $P < 0.05$). This dysfunction coincided with a significant rise in cellular senescence hallmarks, including increases in lysosomal alteration, as indicated by SA- β -gal positivity (Fig. 1m), and the expression of cyclin-dependent kinase (CDK) inhibitor p16^{INK4a} (Fig. 1n) and SASP component VCAM1 (Fig. 1o) in aortic ECs. Additionally, DNA damage response, represented by increased γ -H2A.X phosphorylation, emphasized cellular senescence phenotype in ECs from aged aortas (Fig. 1p).

The strong association between age-related PAA elevation, *Clostridium* genus (seen in both aged humans and mice), particularly *Clostridium* sp. ASF356 and vascular dysfunction highlights the key role of gut bacteria in phenylalanine metabolism and its impact on endothelial biology and vascular decline in aging.

Clostridium sp. ASF356 triggers endothelial senescence in vivo

To explore whether *Clostridium* sp. ASF356, by elevating PAA, causally triggers aortic endothelial senescence and dysfunction in young mice, mirroring observations in aged mice, we colonized antibiotics (ABx)-pretreated mice with *Clostridium* sp. ASF356 (*Clos*) via oral gavage for 4 weeks (Fig. 2a). PCR confirmed successful colonization, as evidenced by a significant increase in *GroEL* gene transcription, which is unique and highly specific to the bacterium and encodes the conserved molecular chaperone GroEL (Supplementary Fig. 2a,c). *Clos* colonization led to a -3.15-fold increase in PAA and -1.7-fold increase in PAGln in plasma (Fig. 2b,c) compared to vehicle-recipient counterparts, confirming the bacterium's ability to metabolize phenylalanine to PAA and PAGln in vivo.

Upon tissue collection, we noted diminished aortic elasticity, concomitant with heightened expression of tissue remodeling biomarkers collagen type III (Col3a1) and matrix metalloproteinase-9 (MMP-9) (Fig. 2d). Additionally, we observed increased vascularity of perivascular adipose tissue (PVAT) and visceral adipose tissue wet weight, both linked to poor cardiovascular outcomes and cardiovascular mortality¹⁹. These observations were corroborated by a senescence-like phenotype in aortic ECs from *Clos*-colonized mice, evidenced by a significant increase in expression of the proliferative arrest marker p16^{INK4a} and DNA damage (γ -H2A.X phosphorylation) (Fig. 2e). The SASP components IL-1 β and its downstream effector IL-6 were also upregulated (Fig. 2f), along with increased SA- β -gal positivity (Fig. 2g). These cellular alterations culminated in a marked decline in vasorelaxation responses,

demonstrated as significantly decreased maximal relaxation at 10^{-5} M acetylcholine (vehicle, 88.53 ± 5.40 ; *Clos*, 77.15 ± 6.66 ; $P < 0.01$), with a nonsignificant rightward shift in EC_{50} (vehicle, 40.57 ± 5.20 nM; *Clos*, 45.77 ± 14.96 nM) (Fig. 2h). Furthermore, angiogenic capacity was reduced, with markedly lower numbers of endothelial sprouts in aortic rings from *Clos*-colonized mice (Fig. 2i).

To confirm whether *Clos* causally promotes EC senescence and dysfunction in vivo, we exploited the potent senolytic D + Q cocktail of 5 mg kg⁻¹ dasatinib (D) + 50 mg kg⁻¹ quercetin (Q) to mitigate EC senescence in *Clos*-colonized mice (Fig. 2j). Our data show that D + Q effectively reverses major senescence hallmarks, as evidenced by reduced expression of p16^{INK4a} and γ -H2A.X (Fig. 2k), IL-1 β and IL-6 (Fig. 2l), and lysosomal SA- β -gal activity (Fig. 2m). This senescence rescue corresponded with restored vascular function, indicated by enhanced endothelial sprouting in aortic rings from treated mice (Fig. 2n). Together, these data provide strong support for a direct contribution of *Clostridium* sp. ASF356 to endothelial senescence in vivo, potentially through enhanced phenylalanine metabolism to PAA.

PAA causally induces premature endothelial senescence

To confirm that PAA directly underpins *Clos*-induced endothelial senescence and angiogenic incompetence, we stimulated proliferating human aortic ECs (p.4–5) with exogenous PAA and compared them to replicative senescent ECs (p.15–17) in vitro (Fig. 3a). PAA-treated proliferating ECs (PEC) exhibited the senescence phenotype (including enlarged, flattened and multinucleated appearance of cells) and associated markers, validated as irreversible proliferative arrest (Supplementary Fig. 3) and exacerbated multiple premature senescence-like parameters such as concomitant increases in numbers of SA- β -gal⁺ cells (Fig. 3b) and expression of γ -H2A.X (Fig. 3c) and CDK inhibitors *CDKN2A* (p16^{INK4a}), *CDKN2D* (p19^{INK4d}) and *CDKN1A* (p21^{WAF1/Cip1}) at messenger RNA level (Fig. 3d), comparable to what seen in replicative SECs. Additionally, PAA markedly reduced the levels of Ki67 signals to the extent seen in SECs, confirming cell-cycle arrest in PAA-exposed PECs (Fig. 3e). Our qPCR assays also demonstrated that PAA significantly increases transcriptional levels of the SASP components, including *IL1A*, *IL1B*, *IL6*, *TNF* and *VCAM1* (Fig. 3f). The latter was also confirmed by VCAM1 immunostaining (Fig. 3g), mirroring observations in aged aortas (Fig. 1n).

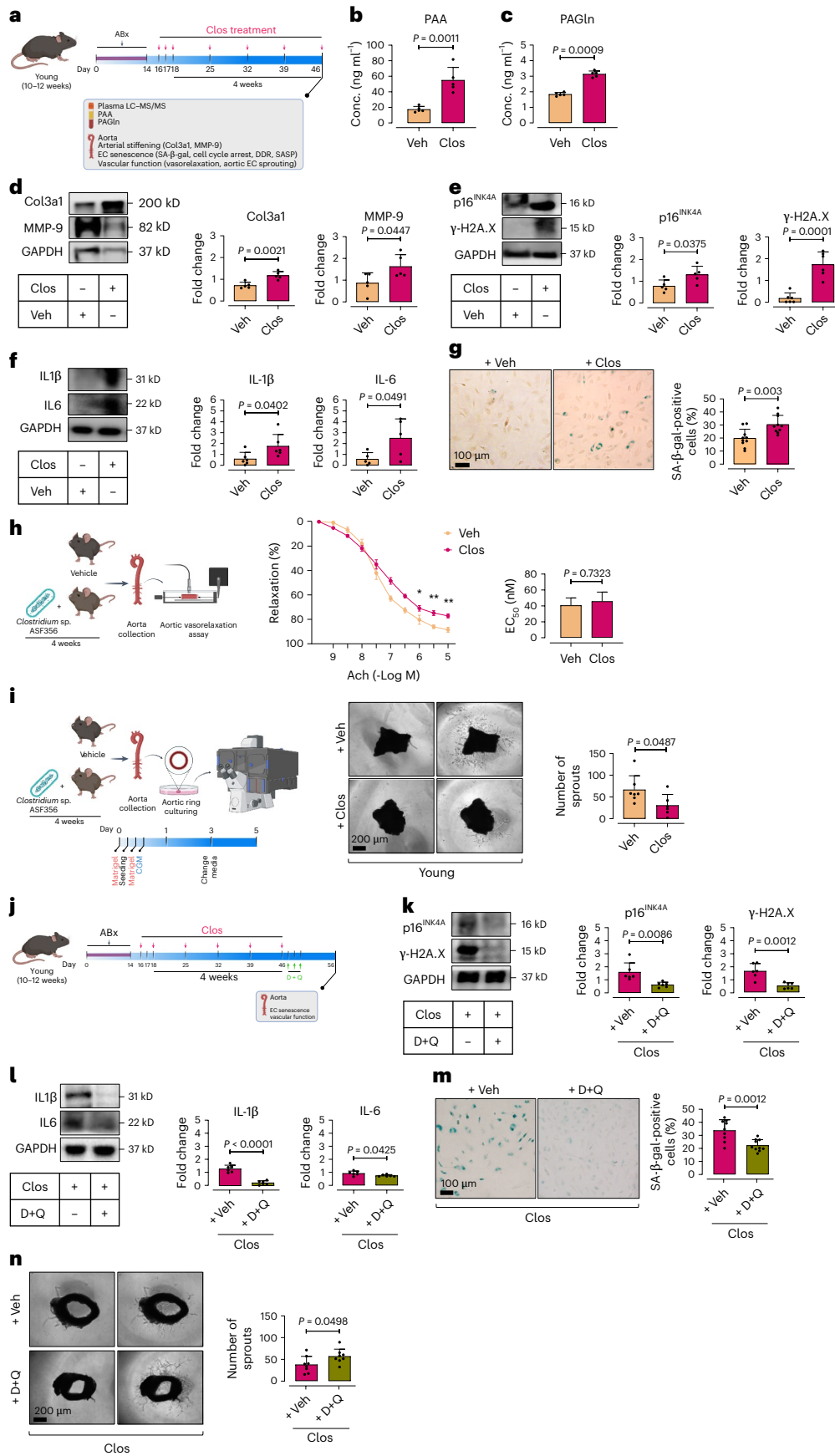
To further support these findings, we conducted in vitro treatment of PECs with PAA (10 μ M, for 72 h), followed by senolytic D + Q (500 nM + 20 μ M, for 24 h) (Extended Data Fig. 2a). Our results demonstrate that D + Q selectively reduced viability of senescent ECs (-67.82%), while sparing proliferating cells (-88.55%) (Extended Data Fig. 2b). Consistently, D + Q significantly increased Ki67⁺ cells and reduced numbers of SA- β -gal⁺ cells (-60.12%) (Extended Data Fig. 2c,d). The selective elimination of PAA-induced senescent ECs subsequently improved endothelial tube formation (-1.5-fold), an in vitro measure of angiogenesis (Extended Data Fig. 2e).

As a proof of concept, we investigated senescence-promoting effects of PAA in vivo (Fig. 3h). Our data revealed that a 4-week PAA

Fig. 2 | *Clostridium* sp. ASF356 induces EC senescence in aortas of colonized mice.

a, Schematic of the experimental setting: 10–12-week-old C57BL/6J male mice were pretreated with antibiotics (ABx) for 2 weeks, then colonized with *Clostridium* sp. ASF356 (*Clos*) by oral gavage for 4 weeks. **b, c**, LC-MS/MS quantification demonstrates plasma PAA (**b**) and PAGln (**c**) levels in mice ($n = 5-6$). **d**, Immunoblotting represents the expression of arterial stiffening biomarkers collagen 3a1 (Col3a1) and matrix metalloproteinase-9 (MMP-9) in aortas of mice ($n = 5-6$). **e-g**, ECs isolated from mouse aortas were subjected to characterization of cellular senescence hallmarks, including proliferative arrest marker p16^{INK4a} and DDR marker γ -H2A.X (**e**), the SASP components IL-1 β and IL-6 (**f**) and SA- β -gal activity (**g**) ($n = 5-6$). **h**, Schematic of ex vivo force tension myography. Aortic rings from *Clos*-colonized mice showed impaired vasorelaxation responses (%) to acetylcholine ($n = 5-6$). **i**, Schematic of aortic endothelial sprouting assays. Confocal micrographs of aortic rings illustrate

angiogenic capacity of ECs. Quantitative plot for numbers of aortic endothelial sprouts ($n = 5-6$) (right). **j**, Schematic of the experimental setting: 10–12-week-old C57BL/6J male mice underwent ABx pre-treatment (2 weeks) and *Clos* colonization (4 weeks), followed by senolytic dasatinib (D) + quercetin (Q) treatment (D, 5 mg kg⁻¹; Q, 50 mg kg⁻¹, daily by oral gavage for 3 consecutive days). **k-m**, Senescence hallmarks, including p16^{INK4a} and γ -H2A.X (**k**), IL-1 β and IL-6 (**l**) and SA- β -gal activity (**m**), were examined in ECs isolated from aortas of mice ($n = 6$). **n**, Confocal micrographs of aortic rings illustrate the effects of D + Q on aortic endothelial sprouting capacity in *Clos*-colonized mice. Quantitative plot for numbers of endothelial sprouts ($n = 8$) (right). Data were determined in eight micrographs and represent triplicated biologically independent experiments (**i, n**). Scale bars, 100 and 200 μ m. Error bars represent s.d. (**b-g, i, k-n**) or s.e.m. (**h**). P values were calculated using a two-tailed unpaired Student's t -test (**b-i, k-n**). Images created with BioRender.com (**a, h-j**). * $P < 0.05$, ** $P < 0.01$.



administration (50 mg kg⁻¹ d⁻¹, i.p.) led to a significant rise in circulating PAA and PAGln levels (Fig. 3i), accompanied by upregulated stiffening markers Col3a1 and MMP-9 (Fig. 3j) in aortas of young mice, mirroring findings in *Clos*-colonized mice (Fig. 2d). Notably, cellular senescence markers were upregulated in aortic cells, evidenced by significant increases in p16^{INK4a} and γ -H2A.X (Fig. 3k), alongside IL-1 β and IL-6 (Fig. 3l) in aortic ECs. The senescent phenotype was associated with impaired angiogenic capacity compared to vehicle-recipient controls (Fig. 3m). Collectively, these findings support a causal role for PAA in driving EC senescence, akin to aging-related endothelial decline.

PAA induces mitochondrial dysfunction via excess H₂O₂

To better understand the mechanism underpinning PAA-induced EC senescence, we observed that PAA triggers premature EC senescence to the magnitude seen in response to exogenous H₂O₂ (Fig. 4a). Since excessive ROS, particularly H₂O₂, are well characterized to trigger EC senescence⁶, we tested whether PAA increases ROS generation. CellRox Green fluorescence imaging confirmed markedly higher global ROS generation in PAA-exposed PEC (Fig. 4b). Using the ultrasensitive H₂O₂ biosensor, HyPer7.2, we detected significant elevation of mitochondrial H₂O₂ in presence of PAA (Fig. 4c). As shown in Fig. 4d, maximal HyPer7.2 ratio in PAA-treated PECs was comparable to that seen with exogenous H₂O₂ (50 μ M). To identify the source of excess mitochondrial H₂O₂, we found that PAA-treated PECs exhibit increased NADPH oxidase 4 (NOX4) expression (Fig. 4e). Meanwhile, glutathione peroxidase (*Gpx1*) transcripts were markedly reduced upon exposure to PAA ('stress condition'), counteracting antioxidant defense (Supplementary Fig. 4).

Altered metabolism is a key driver of endothelial senescence²⁰, so we tested mitochondrial function, impairment of which aggravates oxidative stress. Our Seahorse mitochondrial stress assay displayed ~two-fold reduction in basal and maximal respiration rates in PAA-exposed PECs to the magnitude seen in SECs (Fig. 4f). Moreover, spare respiratory capacity, with FCCP-stimulated oxidative phosphorylation (OXPHOS) uncoupling, along with ATP biosynthesis was impaired in response to PAA (Fig. 4f). In agreement with reduced mitochondrial respiration, PAA markedly reduced basal extracellular acidification rate (ECAR), indicating glycolytic decline (Fig. 4g), a major energy supplier in ECs²¹.

PAA triggers endothelial senescence by epigenetic alterations

Senescence involves extensive epigenetic reprogramming, including histone modifications that alter gene expression patterns^{4,22}. Histone deacetylase 4 (HDAC4) is an epigenetic regulator of cellular senescence²³, modulated by post-translational modification partly regulated by NOX4-derived H₂O₂ in ECs²⁴. Accordingly, we tested whether PAA, which earlier was shown to induce mitochondrial H₂O₂ generation (Fig. 4b–d), impacts HDAC4 and epigenetic responses, rendering EC senescence.

In line with Fig. 3f, PAA significantly increases IL-6 expression at a protein level in PECs, comparable to those in SECs (Fig. 5a,b). As

shown in Extended Data Fig. 3a–f, chemogenetic H₂O₂ (by D-amino acid oxidase (DAAO) in presence of D-alanine²⁵) upregulates IL-6, confirming that PAA-mediated SASP is H₂O₂-dependent. As CaMKII is a both H₂O₂- and IL-6-responsive protein kinase that regulates HDAC4 phosphorylation²⁴, we assessed how PAA regulates the CaMKII–HDAC4 pathway. Our findings revealed that PAA significantly increases phosphorylation of CaMKII at Thr286 and its downstream HDAC4 at Ser632 in PECs (Fig. 5a,c,d). As a proof of concept, treatment of PECs with human recombinant IL-6 (hrIL-6) replicated these effects, confirming PAA's role in IL-6–CaMKII activation (Extended Data Fig. 4a,b). Using siRNA against CaMKII, we observed a marked reduction in HDAC4^{S632} phosphorylation in PAA-exposed PECs (Extended Data Fig. 5a–c). Increased HDAC4 phosphorylation facilitates its nuclear export toward the cytosol, evidenced by lower nuclear HDAC expression rather than the cytosolic form (Fig. 5h). Our immunostaining confirms that PAA elicits cytosolic localization of HDAC4 (Fig. 5i), as similarly seen in response to intracellular H₂O₂ generated by DAAO (Extended Data Fig. 6a,b).

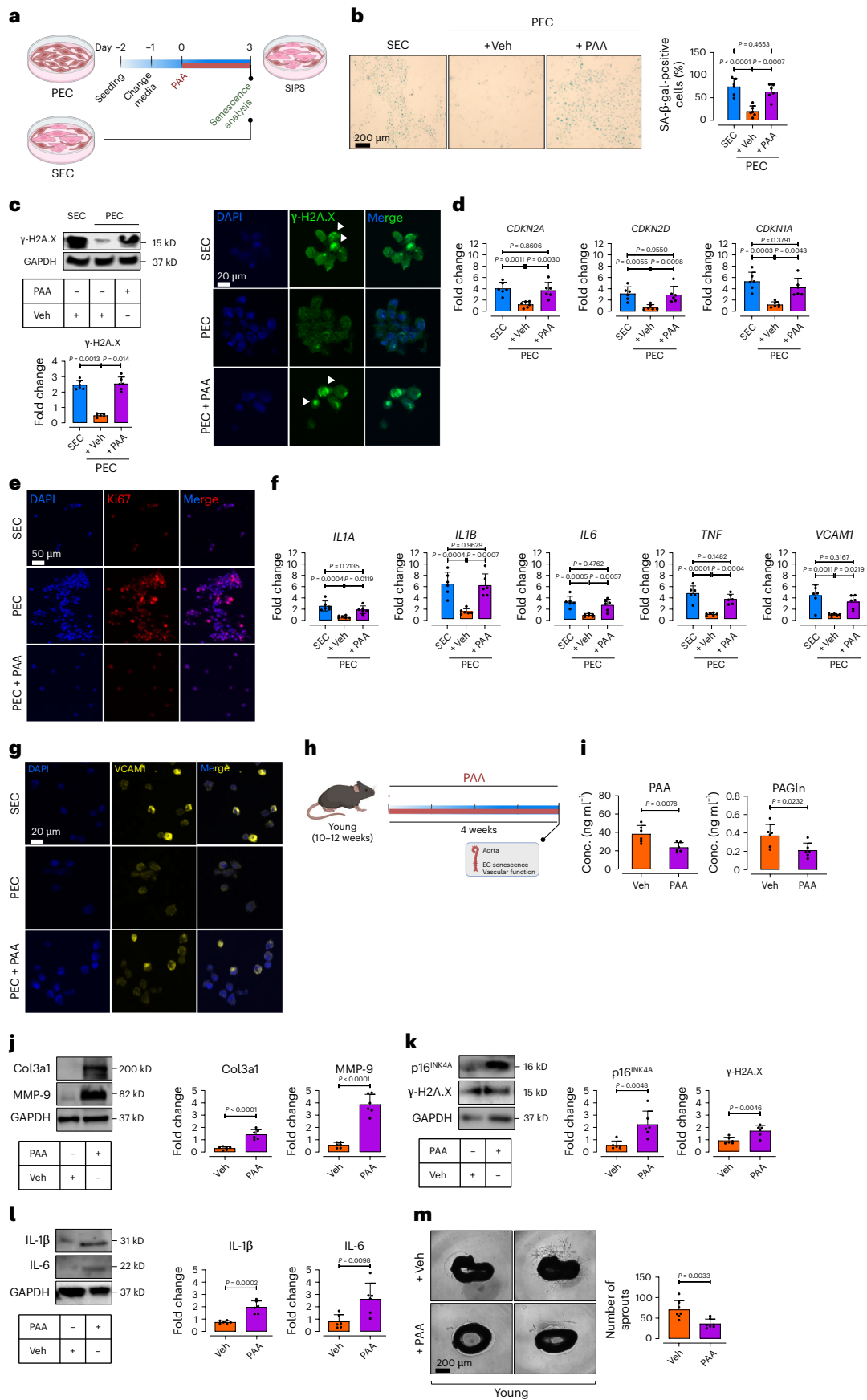
One major downstream of HDAC4 contributing to endothelial dysfunction is the SASP component VCAM1 (ref. 26). Our findings demonstrated that PAA triggers VCAM1 expression at both mRNA (Fig. 3f) and protein (Fig. 5a,e) levels in PECs. Furthermore, PAA-exposed PECs exhibited reduced eNOS^{Ser1177} phosphorylation (Fig. 5a,f), whereas phosphorylation at Thr495 was robustly increased (Fig. 5a,g). To confirm VCAM1's role in regulating eNOS signaling, siVCAM1 transfection of PAA-treated PECs showed that VCAM1 silencing significantly restores eNOS activation (phosphorylation at Ser1177) (Extended Data Fig. 5d). These confirm causal contribution of PAA to endothelial dysfunction through VCAM1 modulation. To test deeply whether H₂O₂ itself underpins PAA-mediated VCAM1–eNOS regulation, we exploited our chemogenetic DAAO model to induce mitochondrial H₂O₂ in PECs. DAAO-generated H₂O₂ in cell mitochondria led to increased VCAM1 expression and suppression of the nitric oxide (NO) signaling axis by eNOS^{Ser1177} dephosphorylation and increased phosphorylation of eNOS^{Thr495} (Extended Data Fig. 3g–i). Similar to outcomes of PAA, chemogenetic H₂O₂ also increased numbers of SA- β -gal⁺ cells (Extended Data Fig. 7a) and γ -H2A.X phosphorylation (Extended Data Fig. 7b,c), confirming H₂O₂ as a driver of PAA-induced endothelial senescence. Our signal transduction studies conclude that PAA causally induces mitochondrial H₂O₂ overproduction, triggering IL-6-mediated HDAC4 cytosolic translocation, which upregulates VCAM1. PAA subsequently disrupts eNOS signaling, leading to vascular dysfunction (Supplementary Fig. 5).

PAA impairs angiogenic capacity of endothelial cells

Because endothelial senescence is linked to impaired angiogenesis, we reasoned that PAA confers critical effects on endothelial angiogenic capacity. Our results show markedly lower migration rates (~two-fold) in PAA-treated PECs at 16 h post-scratch (Fig. 6a). Tube formation assay also demonstrated a ~fourfold reduction in numbers of tubes formed

Fig. 3 | PAA induces endothelial cell senescence. **a**, Schematic diagram of the experimental setting: PECs at p4–5 were treated with PAA (10 μ M) for 72 h and then subjected to senescence hallmarks profiling. **b**, SA- β -gal staining shows senescence-associated lysosomal alterations in PECs treated with PAA versus vehicle versus replicative SECs. Quantitative plots are shown for SA- β -gal-positive cells (%) ($n = 6$) (right). **c**, Immunoblots (top) and γ -H2A.X immunostaining (bottom) represent DDR ($n = 6$). **d**, qPCR shows transcriptional changes of CDK inhibitors *CDKN2A*, *CDKN2D* and *CDKN1A* ($n = 6$). **e**, Immunostaining reveals the expression of proliferation marker Ki67 ($n = 6$). **f**, qPCR demonstrates transcriptional alterations of SASP genes *IL1A*, *IL1B*, *IL6*, *TNF* and *VCAM1* ($n = 6$). **g**, VCAM1 immunostaining shows its expression in ECs ($n = 6$). Data from in vitro cellular experiments represent triplicate biologically independent experiments. **h**, Schematic diagram of the experimental setting: 10–12-week-old C57BL/6J male mice were treated with PAA (50 mg kg⁻¹) via daily

intraperitoneal (i.p.) injections for 4 weeks. Aortas were collected for characterization of EC senescence and angiogenic capacity. **i**, Plasma levels of PAA (left) and PAGln (right) were quantified by LC–MS/MS in mice ($n = 6$). **j–l**, Immunoblots represent the expression of tissue remodeling markers Col3a1 and MMP-9 (**j**) and senescence hallmarks including p16^{INK4a} and γ -H2A.X (**k**) and IL-1 β and IL-6 (**l**) in mouse aortas ($n = 6$). **m**, Confocal micrographs of aortic rings illustrate angiogenic incompetence in PAA- versus Veh-treated young mice. Quantitative plot represents the number of aortic endothelial sprouts ($n = 8$) (right). Data were determined in eight micrographs and represent triplicated biologically independent experiments. Scale bar, 20, 50 and 200 μ m. Error bars represent s.d. (**b–d,f,i–m**). *P* values were calculated using one-way ANOVA followed by Tukey's post hoc test (**b–d,f**) and a two-tailed unpaired Student's *t*-test (**j–m**). Images created with [BioRender.com](https://www.biorender.com) (**a,h**).



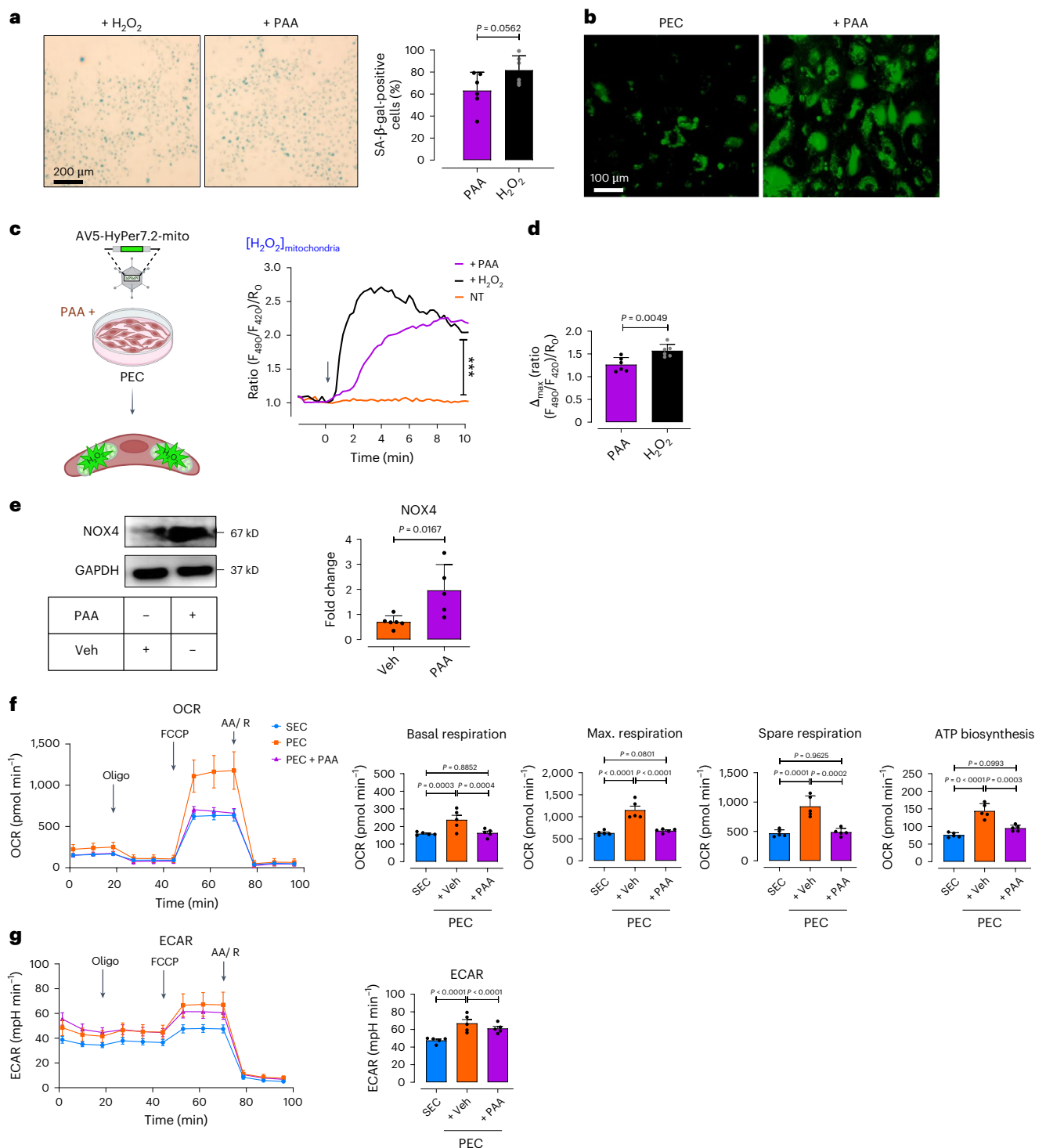


Fig. 4 | PAA regulates premature EC senescence by H_2O_2 -mediated mitochondrial impairment. **a**, SA- β -gal staining shows senescence-associated lysosomal alterations in Veh-treated PECs compared to PECs incubated with exogenous H_2O_2 (50 μM). Quantitative plots for SA- β -gal-positive cells (%) are shown ($n = 6$). **b**, CellRox Green staining reveals the generation of intracellular ROS, including H_2O_2 , (as green fluorescence) in the presence or absence of PAA. **c**, Schematic diagram of the experimental setting: PECs were transduced with adenovirus 5 (AV5)-HyPer7.2 targeted to the cell mitochondria for further ratiometric fluorescence imaging to detect mitochondrial H_2O_2 generation in the presence of PAA. Right, the curves demonstrate significantly higher H_2O_2 responses in the mitochondria of HyPer7.2-transfected PECs following treatment with either PAA ($n = 25$) or exogenous H_2O_2 ($n = 27$) compared to vehicle ($n = 24$). **d**, Bar chart shows maximal mitochondrial H_2O_2 responses to PAA or exogenous H_2O_2 ($n = 6$). **e**, Immunoblot analysis demonstrates the expression of NOX4 in

PECs ($n = 5-6$). **f**, Mitochondrial respiratory rates in PECs treated with either PAA or vehicle and in replicative SECs were measured using Seahorse flux analyzer by Cell Mito Stress kit ($n = 5$). Bar charts reveal oxygen consumption rate (OCR) represented by maximal, basal, and spare reserve, and ATP biosynthesis in PAA-exposed PECs compared to PECs incubated with vehicle. **g**, Glycolysis was measured by ECARs in vehicle- or PAA-treated PECs and replicative SECs under basal conditions ($n = 5$). Bar chart depicts ECAR in Veh-treated PECs compared to PAA-exposed PECs or replicative SECs (right). Data from in vitro cellular experiments represent triplicate biologically independent experiments. Scale bars, 100 and 200 μm . Error bars represent s.d. (**a, d-g**) or s.e.m. (**c, f, g**). P values were calculated using a two-tailed unpaired Student's t -test (**a, e**), two-tailed Mann-Whitney U -test (**d**) and one-way ANOVA followed by Tukey's post hoc test (**c, f, g**). Images created with [BioRender.com](https://www.biorender.com) (**c**). *** $P < 0.001$.

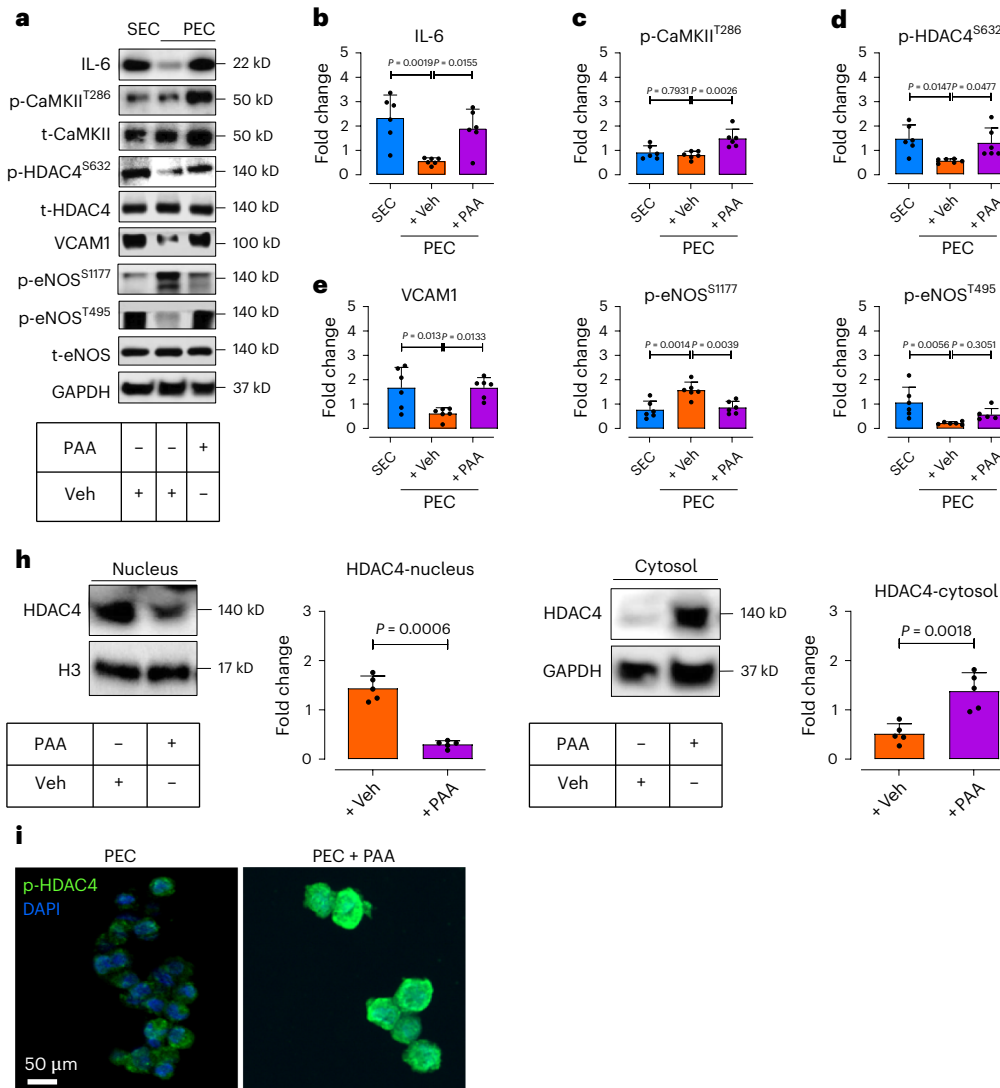


Fig. 5 | PAA induces EC senescence through the SASP-epigenetic regulation. a–g. Immunoblotting represents the expression of IL-6 (b), CaMKII-mediated phosphorylation of HDAC4 at Ser632 (c,d), VCAM1 expression (e), post-transcriptional modifications of eNOS at Ser1177 and Thr495 (f,g) in response to PAA in PECs (n = 6). **h.** Immunoblots and quantitative plots reveal translocation of HDAC4, represented as decreased expression in the nucleus (left) and increased expression in the cytosol (right) in PECs in response to PAA (n = 5).

i, p-HDAC4 immunostaining illustrates HDAC4 phosphorylation, facilitating its translocation toward the cell cytosol in PECs exposed to PAA (n = 6). Scale bar, 50 μm. Data from in vitro cellular experiments represent triplicate biologically independent experiments. Error bars represent s.d. (b–h). P values were calculated using one-way ANOVA followed by Tukey’s post hoc test (b–g) and a two-tailed unpaired Student’s t-test (h).

following PAA treatment, indicating compromised angiogenic capacity (Fig. 6b). In agreement with these data, aortic rings from young mice, incubated with PAA, exhibited markedly attenuated endothelial sprouting, mirroring aged aortas (Fig. 6c). Sprouted aortic rings were also immunostained for endothelial-specific adhesion molecules VE-cadherin (VEC) and CD31. Imaging data confirm a significant reduction in total volume of sprouted VEC⁺, CD31⁺ ECs in response to PAA (Supplementary Fig. 6).

These findings highlight PAA as a key driver of endothelial angiogenic incompetence, mediated through diverse senescence-promoting mechanisms, including SASP, epigenetic modifications and energy imbalance (Supplementary Fig. 7).

Acetate rescues PAA-induced endothelial senescence as a senomorphic

Aging disrupts gut microbiota balance toward detrimental metabolites and reduction in health-promoting SCFAs^{15,27} such as acetate, which may counteract vascular senescence. Corroborating our previous

findings¹⁵, fecal acetate levels were markedly lower in aged mice compared to young counterparts (Fig. 7a). To test acetate’s anti-senescence potential, we treated PAA-exposed PECs with sodium acetate (3 μM, for 72 h) (Fig. 7b). As anticipated, acetate rescued proliferation, evidenced by significant reduction in *CDKN2A* and *CDKN2D* transcripts (Fig. 7c) and increase in Ki67 signals (Fig. 7d). Additionally, sodium acetate suppressed SASP components *IL1B* and *IL6* (Fig. 7e), triggered by PAA. Beyond its senomorphic effects, sodium acetate mitigated other senescence hallmarks, shown as reduced SA-β-gal⁺ cells (Fig. 7f), and reversed senescence-associated morphological transformations (Supplementary Fig. 3b). Sodium acetate further counteracted PAA-induced telomere shortening by upregulating hTERT (telomerase reverse transcriptase) expression (Fig. 7g), while reducing DNA damage by γ-H2A.X phosphorylation (Fig. 7h).

To investigate the potential effects of acetate on intracellular ROS sources driving senescence in PAA-exposed ECs, we also examined whether acetate could attenuate mitochondrial ROS production, and through this, restore mitochondrial function. These findings

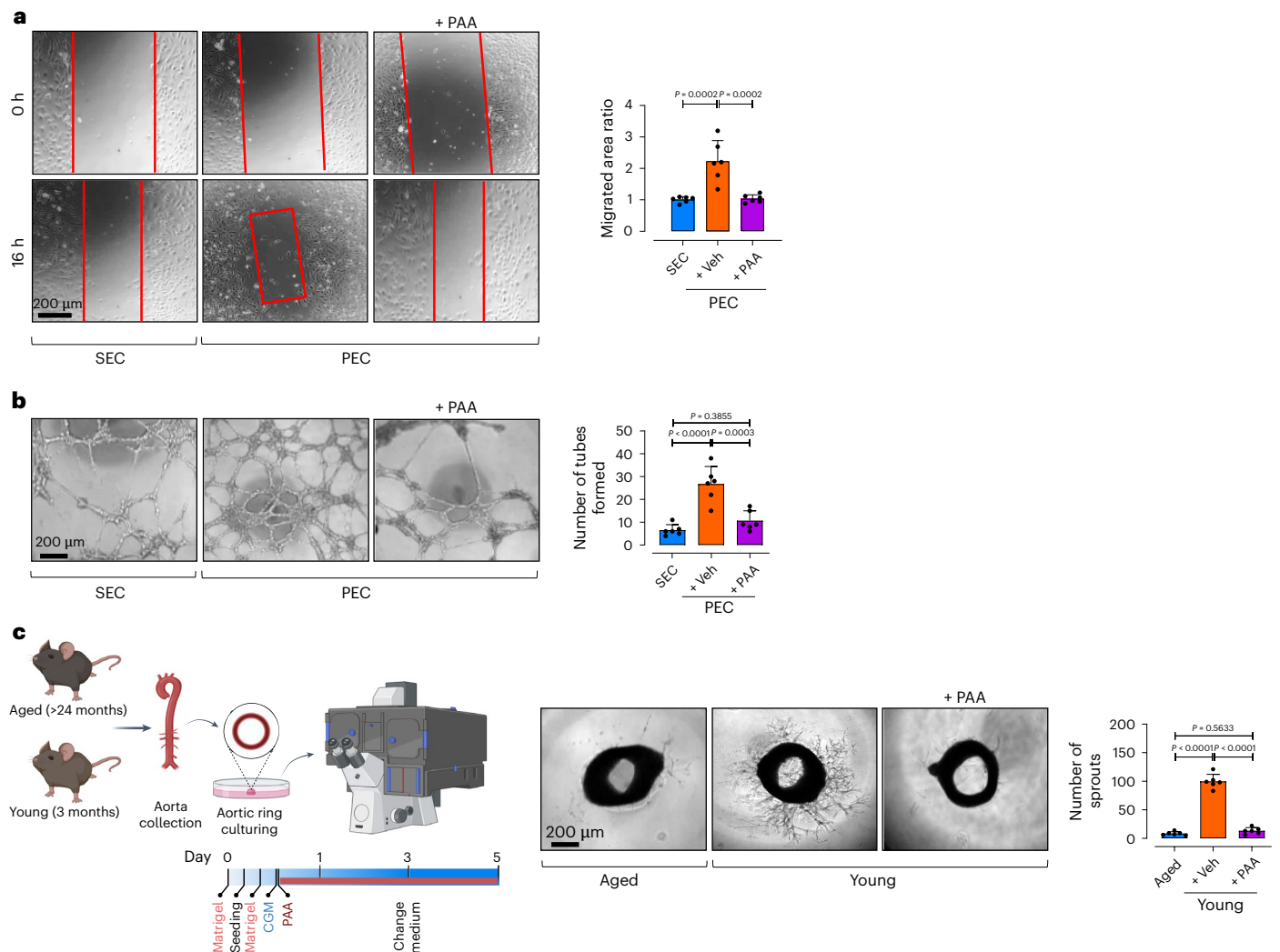


Fig. 6 | PAA reduces EC proliferation and angiogenesis. a, Confocal micrographs depict cell migration, represented as areas of uncovered surface, in PECs treated with PAA or vehicle and in replicative SECs. Bar chart represents the ratio of cell migrated area ($n = 6$) (right). **b**, Confocal images represent two-dimensional Matrigel tube formation of ECs. Quantitative plot shows numbers of tubes formed

by ECs ($n = 6$) (right). **c**, Confocal micrographs of aortic rings from aged and young mice represent angiogenic capacity in response to PAA or vehicle. Quantitative plot is shown for numbers of aortic endothelial sprouts ($n = 6$) (right). Error bars represent s.d. (a–c). P values were calculated using one-way ANOVA followed by Tukey's post hoc test (a–c). Image created with [BioRender.com](https://www.biorender.com) (c).

hold notable therapeutic relevance for acetate to mitigate oxidative stress-induced EC dysfunction. Sodium acetate prevented mitochondrial oxidative stress, evidenced by lower numbers of CellRox⁺ cells in presence of PAA (Fig. 7i). Consistently, sodium acetate improved mitochondrial dysfunction, shown as ~30–40% increase in basal and maximal respiration rates and spare respiratory capacity (Fig. 7j,k). Moreover, ATP was biosynthesized at a significantly higher level in PAA-exposed PECs when supplemented with sodium acetate (Fig. 7k). Notably, acetate serves as a crucial precursor for acetyl-CoA, sustaining the TCA cycle and maintaining redox homeostasis¹⁷. Disruption of this balance by excessive ROS can deplete NAD⁺ levels, and compromise vasculoprotective metabolites²⁸. Acetate effectively alleviates mitochondrial oxidative stress (Fig. 7i) and restores energy homeostasis (Fig. 7j,k), accompanied by increased conversion of acetate into acetyl-CoA (Fig. 7l) through activation of acetyl-CoA synthetase (ACSS2; Fig. 7m). Mitochondrial enzymes, including isocitrate dehydrogenase 2 (IDH2), are also upregulated (Fig. 7m) as part of mitochondrial adaptation. While IDH2 contributes to NAD⁺ consumption to generate NADH, acetate-driven enhancement of oxidative phosphorylation

(Fig. 7j,k), creates a feedback loop where NADH is rapidly oxidized to regenerate NAD⁺ (Fig. 7n and Supplementary Fig. 8). As a proof of concept, pharmacological inhibition of mitochondrial complex I with rotenone reduced acetate-driven NAD⁺ elevation, confirming its dependence on electron transport chain (ETC) activity (Supplementary Fig. 9a,b). The resulting NAD⁺ boost could activate Sirt1, a key NAD⁺-dependent deacetylase, which plays a central role in mitigating oxidative damage and SASP suppression²⁸.

Our mechanistic studies revealed that sodium acetate both mitigates oxidative stress and dampens SASP induced by PAA. Sodium acetate exerts antioxidant effects through Sirt1-mediated stabilization of nuclear factor erythroid 2-related factor 2 (Nrf2), a master regulator of an array of antioxidant enzymes⁶. PAA alone suppressed Sirt1 and its downstream Nrf2 (Extended Data Fig. 8a,b), likely through mitochondrial H₂O₂-induced oxidative stress, while acetate restored nuclear Nrf2 expression in these cells (Fig. 7o). Our loss-of-function studies highlighted that acetate's role in Nrf2 translocation is Sirt1-dependent, as siSirt1-transfected PAA-PECs showed reduced nuclear Nrf2 (deacetylated form) expression (Extended Data Fig. 9a,b). Acetate-mediated

nuclear Nrf2 retention secures its binding to antioxidant responsive elements (AREs), upregulating mitochondrial ROS-neutralizing enzymes *Gpx1*, *Gpx4*, *Prdx3*, *Txn1* and *Txn2*, while pharmacological Nrf2 inhibitor ML385 (5 μ M for 24 h) markedly attenuated acetate's effects in PECs (Fig. 7p). Beyond redox regulation, sodium acetate modulated SASP responses by upregulating Sirt1-mediated epigenetic responses, which suppressed NF- κ B signaling. Sodium acetate specifically facilitated Sirt1 recruitment, leading to reduced NF- κ B RelA/p65 acetylation at Lys310, thereby repressing target gene encoding the SASP component IL-6 in PAA-exposed PECs (Fig. 7q). Sirt1 silencing reversed this effect, confirming its dominant role in NF- κ B deacetylation (Extended Data Fig. 10a,b). As a proof of concept, RelA/p65 knockdown suppressed IL-6 expression, validating NF- κ B's role in SASP regulation (Extended Data Fig. 10c).

Together, these findings identify sodium acetate as a potent senomorphic agent that mitigates PAA-induced endothelial dysfunction through a mechanism distinct from PAA's mechanism in HDAC4-regulated SASP activation. Sodium acetate exerts its effects on redox homeostasis and SASP by restoring NAD⁺-Sirt1 homeostasis, enhancing Nrf2-driven antioxidant defense and suppressing NF- κ B-mediated SASP in the presence of PAA (Supplementary Fig. 10).

Acetate reverses PAA-induced angiogenic incompetence

To determine whether sodium acetate reverses PAA-induced endothelial dysfunction, we assessed its effect on endothelial angiogenic competence. We demonstrated that sodium acetate enhances the transition of PAA-induced senescent ECs toward an angiogenic phenotype, evidenced by restored migration ability (Fig. 8a) and increased numbers of tubes formed to the magnitude of Veh-PECs (Fig. 8b). Moreover, sodium acetate significantly enhanced endothelial sprouting *ex vivo* in PAA-exposed aortic rings (Fig. 8c). Notably, sodium acetate increased numbers of sprouted VEC⁺, CD31⁺ ECs, supporting its role in angiogenesis restoration (Supplementary Fig. 6a,b). As a proof of concept, we tested acetate's capacity in restoring endothelial function in a more complex system, including aortas from *Clos*-colonized mice (Fig. 8d). As expected, our findings mirrored the responses to PAA. Accordingly, sodium acetate significantly reduced senescence hallmarks, p16^{INK4a} and SA- β -gal positivity (Fig. 8e,f), and augmented angiogenic potential, as evidenced by increased numbers of endothelial sprouts (Fig. 8g). These findings suggest that pro-angiogenic effects of acetate supplementation stem from its senomorphic properties, which effectively counteract PAA-induced endothelial senescence and restore endothelial function.

Discussion

In this study, we confirmed a causal link between gut microbiota and aortic endothelial senescence, identifying *Clostridium* sp. ASF356 and its byproduct PAA as contributors to vascular dysfunction. Our

combined metagenomic and metabolomic studies revealed that age-related increases in plasma PAA levels correlate with *ppfor* gene homologs in the aged microbiome. Of note, *Clostridium* sp. ASF356, enriched in aged microbiomes, harbors the *ppfor* gene, facilitating oxidative decarboxylation of phenylpyruvate to PAA, which we confirmed in both *in vivo* and *in vitro* models. Functionally, *Clostridium* sp. ASF356 and its metabolite PAA induce endothelial senescence by inducing SASP and epigenetic alterations. Our senolytic D + Q therapy provided a proof of concept for causal contribution of the metaorganismal metabolite to endothelial senescence and dysfunction and angiogenic incompetence. Therefore, abundance of *Clostridium* sp. ASF356 in microbiome or PAA could be introduced as potential key vascular aging biomarkers. Beyond identifying PAA as a pro-senescent metabolite, we also suggest sodium acetate as a potential senomorphic compound that strongly mitigates SASP, restores mitochondrial redox and energy balance, and thereby improves endothelial function. These findings highlight acetate's senotherapeutic potential for preserving vascular health in aging.

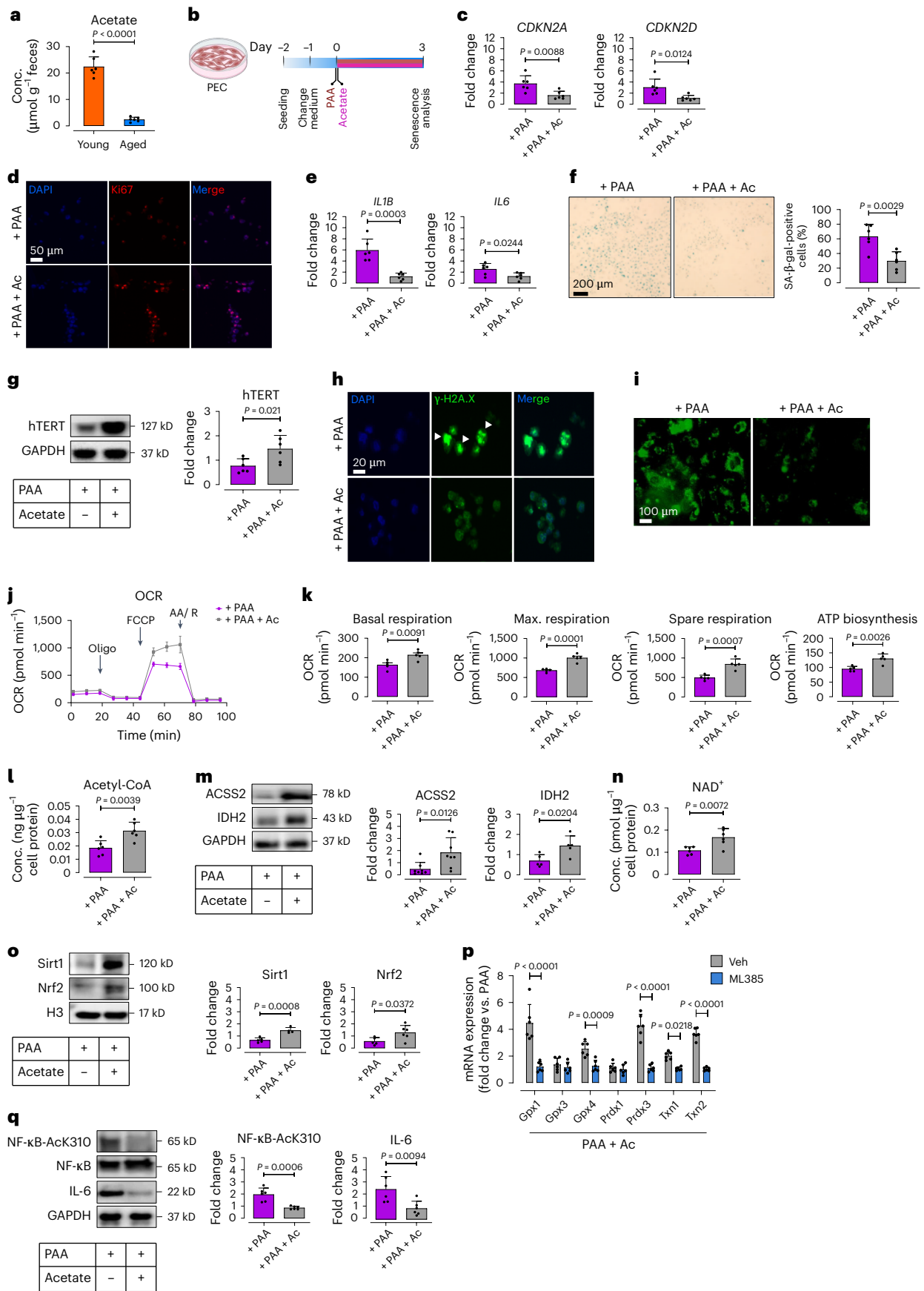
PAA has primarily been recognized as a precursor in the biosynthesis of PAGln in humans¹⁰ and phenylacetylglycine (PAGly) in rodents¹⁸. The formation of PAA occurs through both oxidative and nonoxidative phenylalanine metabolism, mediated by PFFOR, VOR and PPDC enzymes. Recent studies have linked PFFOR and PPDC to atherosclerotic CVD¹⁰. Furthermore, preclinical and clinical studies demonstrated a positive association between PAGln and conditions such as heart failure⁴¹, thrombotic events¹⁰ and, notably, cellular senescence²⁹. The latter is driven by mitochondrial dysfunction and DNA damage in aged mice. These findings complement our study by supporting the involvement of gut microbiota in driving vascular aging. While only one human study has reported an association between PAA and major adverse cardiovascular events in cardiac patients³⁰, the mechanistic implications of PAA remain elusive. Our study establishes a causal role for *Clostridium* sp. ASF356 and its metabolite PAA in driving endothelial senescence and dysfunction, using both mouse and human data. Consistently, our mouse model shows a positive association between *Clostridium* sp. ASF356 and plasma PAA, mirroring findings from TwinsUK cohort, where PAA levels correlated with *Clostridium* spp. expressing *ppfor* gene. Given the functional conservation of key metabolic pathways between human and mouse microbiomes, we propose that *Clostridium* sp. ASF356 or a functionally equivalent taxon may contribute to vascular aging in humans. Future studies employing genomic insights and targeted culturing will enable us to confirm this hypothesis.

Our findings suggest that *Clostridium* sp. ASF356 regulates circulating PAA levels, thereby promoting aortic stiffening and endothelial senescence and dysfunction. Mechanistically, PAA confers its senescence-promoting effects through excessive NOX4-dependent mitochondrial H₂O₂ generation, leading to DNA damage (γ -H2A.X phosphorylation), upregulation of SASP components (IL-1 β and IL-6)

Fig. 7 | Acetate rescues PAA-induced EC senescence through senomorphic effects.

a, Bar charts represent fecal acetate levels in aged mice compared to young mice, as quantified by HPLC-RI ($n = 6$). **b**, Schematic of experimental setting. PECs were co-treated with PAA (10 μ M) and sodium acetate (3 μ M) for 72 h, followed by senescence analysis. **c**, qPCR analyses reveal transcriptional changes of CDK inhibitors *CDKN2A* and *CDKN2D* ($n = 6$). **d**, Ki67 immunostaining represents its expression ($n = 6$). **e**, Bar charts represent transcriptional changes of the SASP components *IL1B* and *IL6*, as assessed by qPCR ($n = 6$). **f**, Representative images of SA- β -gal staining (left) and bar chart (right) demonstrate senescence-associated lysosomal alterations ($n = 6$). **g**, Immunoblots reveal the expression of hTERT, indicating telomere length restoration ($n = 6$). **h**, Representative immunostaining images show γ -H2A.X foci, as a DDR marker ($n = 6$). **i**, CellRox Green staining demonstrates intracellular ROS generation ($n = 6$). **j,k**, Seahorse bioenergetic analysis reveals mitochondrial OCR in PAA- versus acetate + PAA-treated PECs. Bar charts show basal and maximal OCR, spare reserve, and ATP production ($n = 5$). **l**, Fluorometric assay

reveals cellular acetyl-coA concentrations ($n = 6$). **m**, Immunoblots represent the expression of acetyl-coA synthetase 2 (ACSS2) and isocitrate dehydrogenase 2 (IDH2) ($n = 5-8$). **n**, Bar charts demonstrate NAD⁺ levels, as quantified by colorimetric assay ($n = 6$). **o**, Immunoblots represent the expression of NAD⁺-dependent Sirt1 and the redox regulator Nrf2 ($n = 5$). **p**, qPCR analysis reveals transcription of the Nrf2-regulated antioxidant enzymes glutathione peroxidase 1 and 4 (*Gpx1* and *Gpx4*), peroxiredoxin 3 (*Prdx3*), and thioredoxin 1 and 2 (*Txn1* and *Txn2*) in PAA + sodium acetate-exposed PECs in the presence or absence of the pharmacological Nrf2 inhibitor, ML385 (5 μ M for 24 h) ($n = 6$). **q**, Immunoblots demonstrate the acetylation level of the heterodimeric subunit of NF- κ B at Lys310, along with the expression of its downstream inflammatory cytokine IL-6 ($n = 6$). Scale bars, 20, 50 and 100 μ m. Error bars represent s.d. (**a,c,e-g,k-q**) or s.e.m. (**j,k**). Data represent triplicate biologically independent experiments. *P* values were calculated using a two-tailed unpaired Student's *t*-test (**a,c,e-g,k-o,q**) and one-way ANOVA followed by Tukey's post hoc test (**p**). Image created with [BioRender.com](https://www.biorender.com) (**b**).



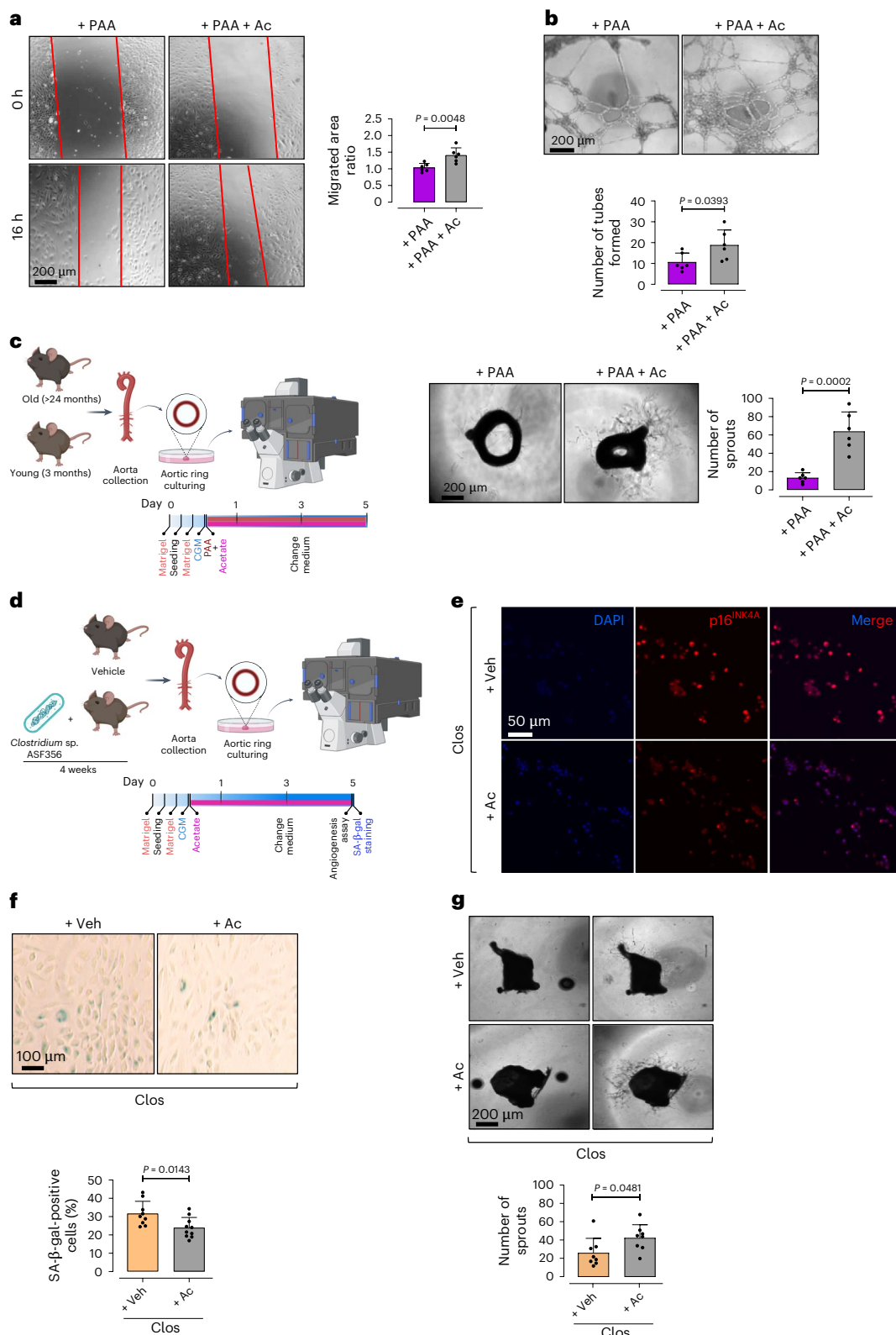


Fig. 8 | Acetate rescues PAA-induced angiogenic incompetence. **a–c**, Confocal micrographs depict the effects of sodium acetate on endothelial angiogenic capacity, represented by cell migration (**a**), tube formation (**b**) and aortic endothelial sprouting (**c**). Quantitative plots represent migrated area ratio (**a**), numbers of tubes formed (**b**) and numbers of endothelial sprouts from aortic rings (**c**) in acetate + PAA-treated group compared to PAA-exposed group ($n = 5–6$). **d**, Schematic diagram of the experimental setting. Aortas were collected from *Clos*-colonized mice for ex vivo aortic EC sprouting assay or isolation of ECs, followed by p16^{INK4A} immunostaining and SA- β -gal staining,

in the presence or absence of sodium acetate. **e, f**, Immunostaining reveals the expression of proliferative arrest marker p16^{INK4A} (**e**) and SA- β -gal positivity, represented as SA- β -gal⁺ cells (%) (**f**) ($n = 5–6$). **g**, Confocal micrographs of aortic rings represent angiogenic capacity in aortas obtained from *Clos*-colonized mice in response to sodium acetate versus vehicle. Quantitative plot is shown for the number of aortic endothelial sprouts ($n = 5–6$) (right). Scale bars, 50, 100 and 200 μ m. Error bars represent s.d. (**a–c, f, g**). Data represent triplicate biologically independent experiments. P values were calculated using a two-tailed unpaired Student's t -test. Images created with BioRender.com (**c, d**).

and proliferative arrest marked by p16^{INK4a}, p19^{INK4d} and p21^{WAF1/Cip1} upregulation. PAA-treated ECs also displayed reduced Ki67 expression and impaired viability, consistent with a senescent phenotype. Notably, PAA-driven senescence extended beyond in vitro models, as it also drives SASP and proliferative arrest in aortic ECs in vivo, resembling vascular changes in aged mice. As a proof of concept, senolytic intervention with D + Q could selectively eliminate senescent ECs triggered by the bacterium or its metabolite PAA, validated by reduced proliferative arrest, SASP, DNA damage response (DDR) and lysosomal alterations. The senescence rescue subsequently led to restoration of endothelial function in *Clos*-colonized mice. These findings align with previous studies demonstrating that senolytic D + Q therapy effectively improves vascular phenotype in aged and hypercholesterolemic mice by targeting senescent endothelial and vascular smooth muscle cells³¹. Furthermore, clearance of senescence cells in aortic atheroma lesions has been previously shown to attenuate atherosclerosis progression in chronologically or accelerated (progeroid *Ercc1*^{fl/fl}) aged mice and athero-prone *Ldlr*-knockout (KO), *3MR* mice fed a high-fat diet^{32,33}.

To delve deeper into the mechanistic significance of PAA in endothelial senescence, we employed a chemogenetic approach using recombinant lentiviral DAAO, which selectively generates intracellular H₂O₂ in mitochondria. Our results confirmed that mitochondrial H₂O₂ induces EC senescence, marked by DNA damage and increased SA- β -gal activity. Aside from this, PAA-induced stress condition counteracts antioxidant defense mechanisms, notably suppressing GPx1, an enzyme essential for H₂O₂ detoxification. In line with previous findings, glutathione peroxidase deficiency promotes p53/p21 pathway activation and endothelial dysfunction, a hallmark of early atherosclerosis³⁴. Thus, we believe that PAA may potentially be a pro-oxidant inducer of EC senescence in aging organisms. Beyond oxidative stress, PAA-exposed ECs developed a persistent proinflammatory phenotype, with increased IL-1 β , IL-6 and VCAM1 expression. Our experiments by exploiting chemogenetic DAAO system verified that mitochondrial H₂O₂ directly upregulates IL-6 and VCAM1, explaining a H₂O₂ dependent fashion for PAA-induced SASP activation. These findings suggest PAA as a potent pro-oxidant metabolite that accelerates EC senescence via SASP induction.

To further explore mechanisms underpinning PAA-induced SASP, we relied upon our previous findings, hypothesizing PAA's role in epigenetic regulation of the SASP components IL-6 and VCAM1 in ECs. We found that PAA-driven H₂O₂ aggravates HDAC4 phosphorylation and cytosolic translocation, leading to VCAM1 de-repression. This aligns with previous reports showing that NOX4-derived H₂O₂ modulates the HDAC4 nucleus–cytosol shuttle through both direct oxidation²⁴ and H₂O₂-regulated phosphorylation³⁵. Our data revealed that PAA-mediated H₂O₂ indirectly boosts CaMKII phosphorylation of HDAC4, reinforcing its cytosolic accumulation. Furthermore, IL-6 upregulation in PAA-exposed senescent ECs coincided with CaMKII phosphorylation, supporting previous evidence that IL-6/sIL-6R signaling activates CaMKII in a JAK/STAT3-dependent manner in human umbilical vein ECs, thereby regulating endothelial motility and proliferation³⁶. Therefore, we believe that PAA both directly (oxidizing by H₂O₂) and indirectly (by activating CaMKII) regulates HDAC4 post-translational modification, leading to VCAM1 de-repression in ECs. We also found that epigenetic regulation of VCAM1 disrupts eNOS signaling, ultimately attenuating angiogenesis. As reported previously, eNOS phosphorylation at Ser1177, but not Thr495, by multiple protein kinases can enhance angiogenesis in ischemic tissues³⁷. Our findings support the contribution of PAA-induced inflammatory environment to angiogenic incompetence. Mechanistically, PAA-driven oxidative stress and SASP disrupt mitochondrial homeostasis and energy supply, further compromising angiogenic capacity. Previous studies demonstrated that ECs rely on fatty acid β -oxidation to sustain the TCA cycle and OXPHOS during angiogenesis¹⁷, while also utilizing glycolysis for migration and proliferation. Consistently, our data reveal that

PAA inhibits both oxidative phosphorylation and glycolysis, leading to an ATP deficit and impaired angiogenesis. Our findings suggest that an age-related increase in PAA drives metabolic alterations that impair angiogenic capacity through the SASP component VCAM1 in ECs. Given that impaired angiogenesis underlies blood supply crisis in aged patients with arterial stiffness, atherosclerosis and ischemic heart disease³⁸, our studies provide a mechanistic basis for PAA as a potential driver of angiogenic incompetence.

To develop a targeted microbiome-based approach against EC senescence, we stand on age-related decline in gut-derived acetate, a key anti-inflammatory SCFA¹⁵. Given its efficacy in counteracting SASP components (IL-1 β and IL-6) in our preliminary studies, we further validated sodium acetate as a potential senomorphic agent in both *Clos*- and PAA-induced EC senescence models. Mechanistically, our findings directed us to the conclusion that acetate drives metabolic reprogramming by activating ACSS2, which converts acetate to acetyl-CoA, fueling the TCA cycle and restoring IDH2 activity, essential for NADH regeneration. This reactivates the ETC and rescues ATP biosynthesis, counteracting PAA-induced metabolic stress. An acetate-driven feedback loop, wherein NADH is rapidly recycled back into NAD⁺, maintains redox homeostasis in these cells. Our supplementary data confirm that acetate-mediated NADH-to-NAD⁺ conversion in PAA-exposed ECs is inhibited by rotenone, a selective complex I inhibitor, underscoring the importance of ETC activity in acetate's role in restoring energy balance. Consistent with previous studies, sodium acetate effectively rescues EC senescence, compensates for cellular energy homeostasis, necessary for restoring angiogenic capacity. These findings align with previous studies unveiling the instrumental role of acetate in rescuing fatty acid β -oxidation in quiescent ECs¹⁷ and providing systemic benefits for ameliorating arterial stiffness³⁹ and hypertension⁴⁰ in aged mice.

In addition to maintaining energy homeostasis, acetate restores redox balance by attenuating ROS accumulation in PAA-exposed ECs. While mitochondrial OXPHOS may indeed elevate ROS levels, the controlled magnitude and kinetics of H₂O₂ production by mitochondrial respiration restricts its capacity to directly induce DNA damage and senescence⁴¹. Notably, our findings demonstrate that acetate concurrently enhances NAD⁺ availability and antioxidant defense mechanisms by upregulating Nrf2-regulated antioxidant enzymes (Gpx1, Gpx4, Prdx3, Txn1 and Txn2), thereby reinforcing redox homeostasis. This aligns with a recent study by Adeyemi et al., showing that acetate activates Nrf2/HO-1 signaling, leading to GPx, catalase and SOD induction, which protects against doxorubicin-induced cardiac oxidative damage⁴². Similarly, in aged mice, sodium acetate suppressed oxidative stress by upregulating glutathione reductase (GRx), Gpx3 and Prdx1, supporting its vasculoprotective effects both in vivo and in vitro¹⁷.

A remaining critical question is how acetate modulates Nrf2-driven antioxidant defense to restore mitochondrial redox homeostasis. Our findings indicate that NAD⁺ plays a pivotal role as both a sirtuin deacetylase substrate and a redox-energy regulator. Loss-of-function studies confirm that sodium acetate upregulates NAD⁺-dependent Sirt1, which in turn both deacetylates and activates Nrf2, facilitating its nuclear translocation in ECs. In contrast, PAA promotes the Nrf2 cytosolic shuttle, impairing its antioxidant function. Pharmacological inhibition of Nrf2 by ML385 confirmed that Nrf2 orchestrates the transcription of downstream antioxidant pathways, neutralizing PAA-induced mitochondrial ROS accumulation. Emerging evidence underscores the interplay between Sirt1/Nrf2 signaling and redox-energy regulation. In replicative senescent human umbilical vein ECs, a decline in OXPHOS and glycolytic capacity is linked to Nrf2 suppression⁴³. Moreover, Nrf2 repression and disruption of Nrf2/ARE antioxidant pathway contribute to progeroid phenotypes, as seen in Hutchinson–Gilford progeria syndrome⁴⁴, while its upregulation boosts metabolic resilience to oxidative and metabolic stress and reduces atherosclerotic burden⁴⁵. Consistently, long-lived animal models exhibit enhanced Nrf2-regulated antioxidant signaling, suggesting that Nrf2 activation may underpin

Table 1 | Plasma PAA and PAGln mass spectrometry conditions

| | Polarity | Formula | Adduct | Precursor ion (m/z) | Product ion (m/z) | HCD (%) |
|----------|----------|--|--------|---------------------|-------------------|---------|
| PAA | Negative | C ₈ H ₈ O ₂ | -H | 135.0452 | 91.0553 | 30 |
| PAA-d5 | Negative | C ₈ H ₃ O ₂ D ₅ | -H | 140.0765 | 96.0869 | 30 |
| PAGln | Negative | C ₁₃ H ₁₆ N ₂ O ₄ | -H | 263.1037 | 127.0513 | 60 |
| PAGln-d5 | Negative | C ₁₃ H ₁₁ N ₂ O ₄ D ₅ | -H | 268.1351 | 127.0513 | 60 |

lifespan extension^{46,47}. In agreement with previous studies, our findings prove that Nrf2's endothelial protection has roots in its upstream regulator, Sirt1. Accordingly, resveratrol, a plant-derived Sirt1 activator, attenuated oxidative stress in coronary arterial ECs and improved vasodilation through Nrf2 activation in mice fed a high-fat diet, whereas its vasculoprotective effects were diminished in Nrf2-deficient mice⁴⁸. A growing number of clinical trials on sirtuin- and NAD⁺-boosting therapies report beneficial effects on arterial stiffening, atherosclerosis and coronary artery disease^{49,50}, underscoring the translational potential of Sirt1/Nrf2-targeting interventions. Given these findings, we believe that reduced abundance of acetate-producing bacteria in aging microbiota may disrupt redox-energy balance. Notably, some studies show that germ-free mice, despite lacking acetate-producing bacteria, exhibit extended healthspan⁵¹, seemingly conflicting with our observations; however, these mice are also devoid of microbial triggers of cellular senescence, such as PAA, PAGln and trimethylamine-*N*-oxide (TMAO), suggesting that the absence of harmful microbial metabolites, rather than acetate depletion, may contribute to their longevity. This highlights the complex interplay between gut microbiota, cellular senescence and host lifespan, reinforcing the need for microbiome-targeted interventions that selectively preserve beneficial microbial metabolites like acetate.

Our studies show that acetate-mediated Sirt1 upregulation not only restores redox and energy balances but also suppresses PAA-induced SASP in ECs. As earlier shown in this work, PAA promotes IL-6-driven VCAM1 signaling, contributing to EC senescence and dysfunction. Our acetate-based intervention identified Sirt1 as a central modulator in reversing these effects. Notably, it has been proposed that Sirt1 deacetylates the RelA/p65 subunit of NF-κB at Lys310, as its direct target, reducing IL-6 expression and attenuating the proinflammatory cascade. These findings align with the targeting aging with metformin (TAME) clinical trial outcomes, where metformin suppresses multiple SASP-associated pathways through Sirt1 activation in diverse cell types such as ECs and adipocytes, extending lifespan and healthspan in humans and mice^{52,53}. Conversely, PAA-induced mitochondrial H₂O₂ accumulation diminishes Sirt1 expression and its deacetylation activity, thereby sustaining NF-κB-driven inflammatory responses. Previous studies confirm that elevated ROS triggers SASP either directly by NF-κB activation or indirectly by ROS-dependent DDR or telomeric damage⁵⁴. Our collective data support this, demonstrating that acetate mitigates DDR, restores telomere length and enhances hTERT expression, likely through mitochondrial H₂O₂ suppression. It may enable PAA-exposed ECs to maintain a high energetic proliferative state, necessary for stimulating angiogenic activity in premature aged ECs⁵⁵. Similarly, resveratrol has been shown to prevent cellular senescence by enhancing telomerase activity in endothelial progenitor cells and vascular smooth muscle cells, via Sirt1-mediated suppression of NF-κB-driven cytokine secretion and upregulation of Nrf2-antioxidant responses in aged nonhuman primates^{56,57}. Additionally, our identification of IL-6 as an upstream regulator of CaMKII-VCAM1 signaling highlights acetate's efficacy in restoring eNOS bioavailability by suppressing the PAA-induced IL-6-VCAM1 axis. Acetate also plays a dual role in replenishing cellular energy and targeting the Sirt1-NF-κB pathway, restoring endothelial sprouting and angiogenic capacity.

One limitation of this study is the absence of direct vascular function assessments like endothelium-dependent vasorelaxation assays. While our ex vivo and in vivo analyses suggest that PAA impacts the vascular aging process, further vascular function and hemodynamic studies are needed to fully characterize PAA-induced endothelial dysfunction. Additionally, while acetate seems to restore endothelial homeostasis, its dose-dependent effects on vascular function require further investigation. Future studies should combine longitudinal microbiome-metabolome profiling with vascular imaging to assess the relevance of *Clostridium* sp. ASF356 and PAA in human vascular aging.

In summary, our findings show that *Clostridium* sp. ASF356, harboring the *ppfor* gene, regulates circulating PAA, a key factor in EC senescence and angiogenic incompetence in aging. We discovered that PAA induces cellular senescence in aortic ECs through H₂O₂-regulated SASP. We propose that sodium acetate acts as a senomorphic and redox-homeostatic agent with pro-angiogenic potential to aid recovery from ischemic vascular diseases in older adults. Additionally, genetic engineering of *Clostridium* sp. ASF356 to deplete the *ppfor* gene could offer a microbiome-based strategy to decelerate vascular aging and prevent related pathologies; however, further development is needed to target EC senescence and vascular dysfunction in aging populations.

Methods

TwinsUK human cohort

Plasma metabolomic profiling. To validate the associations between circulating PAA and PAGln concentrations and age, we used the metabolomic data of TwinsUK human aging cohort. The TwinsUK cohort encompasses metabolome data of 1,116 metabolites (including PAA and PAGln) profiled in more than 14,000 adult twins of the same sex between 18 and 95 years old. All participants received no compensation and provided written informed consent. The study was approved by the NRES Committee London-Westminster (REC reference no. EC04/015).

Fecal metagenomic profiling. Stool samples were provided by randomly selected twin participants in the TwinsUK cohort, collected at home and stored at -80 °C at St. Thomas' Hospital for further DNA extraction and library preparation⁵⁸. DNA samples, in multiple batches, were transferred to GenomeScan, Netherlands, for DNA sequencing. Paired-end reads were processed with YAMP (v.0.9.5) using the 'genomescan' parameters. Samples with <10 M paired-end reads were discarded to maintain the quality. The taxonomic profiling and quantification of organisms' relative abundances of all metagenomic samples were quantified using MetaPhlAn v.4.0 (ref. 59). The updated species-specific database of markers was built using 99,237 reference genomes representing 16,797 species retrieved from GenBank (January 2019). From this set of reference genomes, we extracted a total of 1,132,166 markers used to profile 13,393 species. This set of species also included 83 species defined by the CAG group approach that were genetically distinct from species represented by isolate genomes and for which the use of unique marker genes limited the potential issues of using metagenomic assemblies reconstructed over multiple samples. Metagenomes were mapped internally in MetaPhlAn v.4.0 against the marker gene database with Bowtie 2 v.2.3.4.3 with the parameter 'very-sensitive'. The resulting alignments were filtered to remove reads aligned with an MAPQ value < 5, representing an estimated probability of the likelihood of the alignments. The associations between microbial features and metabolites were analyzed using the R package 'lmerTest'.

Mouse models

Our research complies with all ethical regulations approved by the Institutional Animal Care and Use Committee at University of Zurich and the Cantonal Ethics Commission Zurich (ZH023/2023 and ZH241/19). Animal care and all experimental protocols were in accordance to the principles of the '3Rs', replacement, reduction and refinement,

according to Directive 2010/63/EU of the European Parliament and of the Council of 22 September 2010 on the protection of animals used for scientific purposes.

All mice were housed in controlled environments in Plexiglass cages under a strict 12-h light–dark cycle at an ambient temperature of 23 ± 1 °C and humidity of $55 \pm 10\%$, and fed standard chow diet (including 19% protein, 61% carbohydrate and 7% fat, D11112201, Research Diets) until 3 (as young) or >24 (as aged) months of age. Mice had access to drinking water and food ad libitum.

Blood and fecal collection and tissue collection

Mice feces were collected and quickly stored at -80 °C for DNA extraction and shotgun metagenomics and quantification of acetate levels.

Mice were killed by CO₂ inhalation in an area separate from the housing facility. Whole blood was collected by cardiac puncture from mice. Plasma was isolated by centrifugation (125g, 8 min, room temperature)¹⁵. An aliquot of blood samples was incubated for 1 h at room temperature and centrifuged (1,500g, 10 min). After blood collection, the heart was perfused for aorta collection.

Mouse creatinine and BUN assays

Serum creatinine and blood urea nitrogen (BUN) were measured using colorimetric detection kits (Cayman Chemical, 700460 and Invitrogen, EIABUN, respectively), according to the manufacturers' instructions. Absorbance was read at 495 nm (for creatinine) and 450 nm (for BUN) with a microplate reader.

Targeted LC–MS/MS analysis of plasma PAA and PAGln levels

PAA and PAGln concentrations in mouse plasma (100 μ l) were quantified by liquid chromatography coupled to a high-resolution mass spectrometer (LC–HRMS). Plasma was extracted with frozen ethanol/methanol (-20 °C) containing internal standards (D5-PAA and D5-PAGln, $0.25 \mu\text{g ml}^{-1}$) and centrifuged (13,000 rpm, 4 °C, 20 min). Supernatants were reconstituted into 100 μ l of water:methanol (90:10) for next centrifugation. Supernatants were separated in a Waters HSST3 column (150 \times 2.1 mm, 1.8 μ m) and analyzed on a Thermo Ultimate 3000 LC system coupled to a Thermo Exploris 120 orbitrap mass spectrometer. Peaks were identified using standards and processed with Tracefinder 3.2 (Thermo Scientific). All MS conditions are detailed in Table 1.

Fecal DNA extraction

Fecal genomic DNA was extracted using the FastDNA SPIN kit (MP Biomedicals, 116540600-CF). Samples were homogenized in MT buffer with FastPrep, centrifuged and the supernatant was mixed with PPS buffer. DNA was purified using a column, dissolved in sterile Milli-Q water, and assessed by a NanoDrop 2000 (Thermo Scientific).

Shotgun metagenomics

Metagenome libraries were generated using a high-quality genomic DNA and libraries were sequenced on an Illumina NovaSeq 6000 PE150 platform (Novogene) with a 250-bp paired-end model.

Taxonomic profiling. Taxonomic profiling was performed using kraken2/Bracken2 (parameters, $-\text{confidence } 0.51$)⁶⁰ against the mouse microbiota genome catalog (CMMG) (<https://ezmeta.unige.ch/CMMG/Kraken2db/cmmg>)⁶¹. Kraken2 profiles were then subjected to Bracken2 for taxonomic refinement using the corresponding database and read length. Bracken2-corrected CMMG read counts were then normalized for reference genome length and loaded together with available reference genomes taxonomy (https://ezmeta.unige.ch/CMMG/Supplementary_Tables_and_Figures/Tables/Table_S4_curated_taxonomy.tsv) into a phyloseq object for data handling. Only the taxa identified in at least two samples with coverage of at least 100 reads in total were considered for further analyses.

Functional profiling. Genomes were screened for presence of K00169 (*vor*) and or K00179 (*ppfor*), the genes encoding the enzymes participated in the phenylalanine metabolism and production of PAA, based on their available KEGG functional annotations (https://ezmeta.unige.ch/CMMG/functional_annotations/mouse/annotations.tsv). The differential abundance of K00169 or K00179 in the identified genome was then added as additional information in the phyloseq object to identify VOR- and/or PPFOR-positive taxa in the microbiome of aged and young mice. The association between the abundance of KO and plasma levels of PAA and PAGln were also characterized by a Spearman correlation analysis.

Community analysis. Microbiota profiles were characterized using α -diversity and β -diversity¹⁵. Hill-d0, 1 and 2 indices represent the richness of detected taxa in aged or young microbiome. Pielou's index (evenness) represents the relative abundance of each taxon in the communities. The influence of age and sex (=cage) was tested on α -diversity and β -diversity metrics using Wilcoxon univariate nonparametric test and permutational multivariate analysis of variance (PERMANOVA) multivariate test. Age- and sex (=cage)-associated differences in taxa or KO abundance were assessed using the CLR by ANCOM.

Fecal acetate quantification

Fecal pellets were homogenized, and supernatants were analyzed using a LaChrom HPLC system (Merck-Hitachi) equipped with a SecurityGuard Carbo-H cartridge (4 \times 3.0 mm, Phenomenex) and a Rezex ROA-Organic AcidH⁺ column (300 \times 7.8 mm, Phenomenex). Separation was performed with a refractive index detector (L-2490, Merck-Hitachi) for analyte quantification. Data were processed using EZChrom A.04.10 (Agilent).

In vitro screening of PAA and PAGln formation by *Clostridium* sp. ASF356

Axenic culture of *Clostridium* sp. ASF356, a strain from the Altered Schaedler Flora, was obtained from M. Wannemuehler at the Iowa State University. *Clostridium* sp. ASF356 was reactivated by a 1% (v/v) inoculation in either brain heart infusion or yeast casitone fatty acids medium anaerobically at 37 °C. Overnight saturated pre-cultures were transferred (1%, v/v) into the fresh medium and cells were grown for 46 h at 37 °C. Bacterial culture supernatants were quantified using LC–MS/MS system. The raw data were processed using Tracefinder 3.2 (Thermo Scientific).

Mouse treatments

In vivo mouse bacterial colonization. The 10–12-week-old, C57BL/6 male mice were administered an antibiotic cocktail (containing 0.5 mg ml^{-1} ampicillin, 0.5 mg ml^{-1} neomycin, 0.25 mg ml^{-1} vancomycin and 0.5 mg ml^{-1} metronidazole) in drinking water for a total of 2 weeks. After 2 days, mice were administered 0.2 ml *Clostridium* sp. ASF356 bacterial suspension by oral gavage inside a biological safety cabinet. For robust colonization, oral gavages were repeated for 3 consecutive days, followed by every 7 days for 4 weeks. Mice were maintained on a sterilized standard chow diet (containing phenylalanine 4.15 g per 100 g; Research Diets) until they were killed for blood collection and tissue collection. To verify the successful colonization, DNA was isolated from fecal content obtained from the distal colon and used for a PCR reaction.

In vivo senolytic therapy of colonized mice. Mice colonized with *Clostridium* sp. ASF356 for 4 weeks, followed by treatment with a senolytic cocktail consisting of dasatinib (5 mg kg^{-1} , Sigma-Aldrich, CDS023389) and quercetin (50 mg kg^{-1} , Sigma-Aldrich, Q4951) by oral gavage daily for 3 consecutive days, followed by a 7-day resting period. Mice were maintained on a sterilized standard chow diet (containing phenylalanine 4.15 g per 100 g; Research Diets) until they were killed for blood and aorta collection.

In vivo PAA administration. Mice were administered PAA (50 mg kg⁻¹ d⁻¹, Sigma-Aldrich, P16621) via intraperitoneal (i.p.) injection daily for 4 weeks. Mice were killed for blood and aorta collection.

Cell line

Primary human aortic ECs (HAECs; Lonza, CC-2535) were cultured in EBM-2 medium (Lonza, 00190860) supplemented with EGM-2 (10% FBS, 2 mM L-glutamine, 100 µg ml⁻¹ penicillin-streptomycin, Lonza, CC-3162/6) at 37 °C, 5% CO₂. Cells at passages 4–5 (proliferating) and 15–17 (replicative senescence) were studied. Cellular senescence was confirmed by proliferative arrest (reduced cell count), SA-β-gal staining and p21^{WAF1/Cip1} immunoblots.

Mouse aortic endothelial cell isolation

Thoracic aortas were excised from mice, cleaned in ice-cold Dulbecco's phosphate-buffered saline (Gibco, 14190144), and digested with collagenase type II (1 mg ml⁻¹, 37 °C, 45 min; Sigma-Aldrich, C2-28). The cell suspension was filtered (70 µm), centrifuged (300g, 10 min) and resuspended in EBM-2 medium with EGM-2 supplements (37 °C, 5% CO₂). Cells (passages 2–3) were used for senescence studies.

Endothelial cell senescence models

Replicative senescence. HAECs (p.4–5) seeded in EGM-2 (5,000 cells per cm²) were passaged every 48 h until the proliferation is suppressed and replicative senescence phenotype is confirmed (SEC; p.15–17). Cellular senescence was verified by SA-β-gal staining and marked reduction in cell count (stained with Trypan blue)⁶². In parallel, another series of cells (p.4–5) cultured in a growth medium for 48 h was identified as a proliferative control (PEC).

H₂O₂-induced premature senescence. To induce premature senescence, PECs (p.4–5) were cultured in EGM-2 (+10% FBS) and treated with exogenous H₂O₂ (50 µM) for 4 h. The culture medium was then replaced and cells were maintained for up to 72 h.

Senescence-associated-β-galactosidase assay. Cultured HAECs were stained for SA-β-galactosidase according to the manufacturer's instructions (Merck Millipore, KAA002). In brief, cells were fixed and stained with x-gal solution overnight at 37 °C. Senescent cells, illuminated as blue-stained cells, were captured under a Leica TCS-SP8 confocal microscope and analyzed using ImageJ software 1.54j (Fiji).

CellRox Green staining

Cells were grown to confluence in growth medium and treated with CellROX Green reagent at a final concentration of 5 µM (Invitrogen, C10444) for 30 min at 37 °C to detect intracellular ROS by a Leica TCS-SP8 microscope, visualized by LAS-X-Office 1.4.6.28433. The fluorescence intensity was evaluated using ImageJ 1.54j.

Lentiviral DAAO-HyPer7.2 transduction

HAECs were transduced with lentivirus-DAAO-HyPer7.2 targeted to cell mitochondria (multiplicity of infection 20–50) in serum-free medium, replaced with 10% FBS medium after 5 h. After 48–72 h, cells were treated with L-alanine (control) or D-alanine (10 mM) to generate mitochondrial H₂O₂ and subsequently subjected to senescence and signaling studies.

HyPer7.2 fluorescence imaging

HAECs were transduced with adenovirus serotype 5 (AV5)-HyPer7.2-mito (multiplicity of infection 1,000)²⁵. Cells were treated with exogenous H₂O₂ or PAA, washed and incubated in HEPES-buffered solution (pH 7.4) for 2 h at 37 °C. Coverslips were mounted on a live-cell imaging platform for real-time fluorescence imaging. The ratiometric HyPer7.2 biosensor was excited at 420 nm and 490 nm, with emission recorded at 530 nm using Metafluor Software (Molecular Devices)^{63–65}. Mitochondrial H₂O₂ was quantified as the R/R₀ ratio (490/420 nm signals).

Cellular acetyl-CoA measurement

Cultured HAECs were washed, scratched and centrifuged (500g, 5 min, 4 °C). Cytosolic extracts were precipitated with perchloric acid, neutralized (6.0 < pH < 8.0) and analyzed for acetyl-CoA levels using an Acetyl-CoA Assay kit (Sigma-Aldrich, MAK039).

Relative NAD⁺ measurement

Cultured HAECs were washed, suspended in NADH/NAD extraction buffer (Sigma-Aldrich, MAK037), and centrifuged (13,000 rpm, 4 °C, 5 min). Supernatant was split for total NAD (NAD_t) and NADH measurement. Absorbance was measured at 450 nm and NAD⁺ levels were calculated as 'NAD_t - NADH'.

Real-time quantitative PCR

Total RNA from cells and aortas was extracted using TRIzol Reagent (Sigma-Aldrich, T9424), according to the standard protocol^{64–66}, for real-time PCR using Power SYBR Green PCR Master Mix (Thermo Fisher Scientific, 4367659). All the primer sequences are listed in Supplementary Table 1.

siRNA transfection

Cells were grown to 70–80% confluence for transfection with specific siRNAs (listed in Supplementary Table 2) using Lipofectamine RNAiMAX transfection reagent (Invitrogen, 13778150). The silencing efficiency was confirmed by immunoblots.

Immunoblotting

Aortic tissues and ECs were lysed in ice-cold RIPA buffer (Thermo Fisher Scientific, 89901) or nuclear and cytoplasmic extraction reagents (Thermo Fisher Scientific, 78835) supplemented with Halt protease and phosphatase inhibitors cocktail (Thermo Fisher Scientific, 78442). Total protein was quantitated using the BCA protein assay kit (Thermo Fisher Scientific, 23225). Equal amounts of proteins (20 µg) were separated in 10% SDS-PAGE gel, followed by electrotransfer and further incubation with specific antibodies. The protein bands were visualized using Amersham Imager 600 (GE Healthcare) and quantitative densitometric analyses were performed using ImageJ 1.54j.

All antibodies used in immunoblotting are listed in Supplementary Table 3.

Opal Multiplex immunofluorescence

Murine aortas and ECs were formalin-fixed and paraffin-embedded. Then, 4-µm tissue sections were stained with primary antibodies (1:100 dilution) using the Opal multiplex immunostaining system (Akoya Biosciences). Staining conditions were optimized using chromogenic DAB detection (Leica Biosystems). Multiplex immunostaining for p-HDAC4^{Ser632}, CD31, p16^{INK4a}, VCAM1, γ-H2A.X^{Ser139} and 4,6-diamidino-2-phenylindole (DAPI) was performed using the Opal 7-Color Automation immunohistochemistry kit on a Leica Bond Rx autostainer. Antibody/fluorophore pairs were spectrally colocalized as per manufacturer recommendations. Slides were scanned using the Vectra Polaris Imaging System, visualized by Phenochart 1.2.0 (Akoya Biosciences).

Seahorse Mito Stress assay

Cells were seeded at 5,000 cells per well in Seahorse XF24 plates (Agilent Technologies). On the experiment day, cells were washed and incubated in culture medium supplemented with 25 mM glucose, 2 mM glutamine and 1 mM pyruvate (pH 7.4). For a standard mitochondrial stress test, oligomycin (1 µM), FCCP (3 µM) and antimycin A/rotenone (0.5 µM each) were sequentially injected to assess oxygen consumption rate (OCR) and ECAR over a 3-min period. At any condition, five consecutive OCR/ECAR measurements were recorded using the Seahorse XFe96 Analyzer (Agilent Technologies). Data were normalized to total protein per well.

Endothelial cell migration assay

Cells were seeded 24 h before treatment and grown to confluence. A cell-free gap was created using a sterile 200- μ l pipette tip, and monolayer migration was monitored⁶². Phase-contrast live-cell imaging (Olympus IX81, Hamamatsu C11440) captured images every 15 min from time point $t = 0$ to $t = 16$ h at $\times 6.4$ magnification in a humidified incubator (37 °C, 5% CO₂). The migrated area ratio at 16 h was quantified using ImageJ 1.54j.

Endothelial tube formation assay

The angiogenic capacity of ECs was assessed by tube formation assay onto Matrigel (Corning 356234) at a subconfluent level⁶². Images were recorded every 15 min for 16 h at $\times 6.4$ magnification using a phase-contrast Olympus IX81 microscope (Hamamatsu C11440 detector, 1 megapixel, 16 bit). Tube formation was analyzed using ImageJ Angiogenesis Analyzer (v.1.54j).

Ex vivo aortic ring sprouting assay

Aortic ring sprouting was assessed by culturing the fragments of murine aortas (2-mm) onto Matrigel and subsequently imaged daily (for 5 days) using an incubator-equipped phase-contrast Olympus IX81 microscope with the Hamamatsu (C11440) detector, followed by the analysis of the number of aortic sprouts⁶².

Aortic sprout immunofluorescence staining

Murine aortic endothelial sprouts on Matrigel were fixed in 4% PFA, permeabilized with 0.25% Triton X-100 and blocked, followed by incubation with primary and secondary antibodies (1:50 to 1:100). Confocal imaging (Leica TCS-SP8) was performed, and nuclei were labeled using DAPI-containing mounting medium for 30 min.

Ex vivo endothelium-dependent relaxation assay

Murine aortas (2 mm) were mounted in a 5-ml organ chamber filled with Krebs-Ringer bicarbonate solution (37 °C, pH 7.4, bubbled with 95% O₂/5% CO₂) and connected to an isometric force transducer (PowerLab 8/30 and LabChart v.7.2.5, AD Instruments) for continuous isometric tension recording (Multi-Myograph 610M, Danish Myo Technology). Concentration-response curves were obtained in responses to increasing concentrations of acetylcholine (ACh, 10⁻⁹ to 10⁻⁵ M; Sigma-Aldrich, A6625)⁶⁶.

Statistics and reproducibility

No statistical methods were used to predetermine sample sizes, but similar sample sizes were used in previous publications^{15,62,66}. In TwinsUK human study, participants that exhibited values below the detection level (0) for PAA or PAGln were considered as not available. Accordingly, PAA and PAGln were measured in plasma samples of 7,303 individuals by Metabolon using a nontargeted UPLC-MS/MS platform. No animals or data points were excluded from experiments or analyses. No method of randomization was used to assign animals to experimental groups. Animals were monitored daily for sickness symptoms and body weight during their lifespan. They were killed immediately at the clinical end point when recommended by veterinary and biological service staff members. The investigators in this study were blinded to the conditions of the experiments, except for oral gavage (for *Clos*, PAA or D + Q administration) to avoid cross-contamination within the groups. n represents the number of samples or animals used. At least three independent triplicated experiments were performed for each experimental setup. Data are expressed as mean \pm s.d. or s.e.m. and $P < 0.05$ was defined as statistically significant.

Statistical analysis was performed using GraphPad Prism 9 (v.9.5.1), R (v.1.26.1) and R package 'lmerTest' (v.3.1.3, function 'lmer'). Comparisons between two groups were conducted using unpaired two-tailed Student's t -test, two-tailed Mann-Whitney U -test and one-way or two-way analysis of variance (ANOVA) with Tukey's post hoc test.

Heatmaps were generated using the vegan v.2.5-5 package (<https://Github.com/vegan>). Spearman rank correlation was used to analyze associations between plasma levels of metabolites and microbial taxa. Multiple group comparisons were tested using Kruskal-Wallis and PERMANOVA was used for analysis of α - and β -diversity. Multiple comparisons and associated P values were false discovery rate corrected. Data distribution was assumed to be normal but this was not formally tested.

Reporting summary

Further information on research design is available in the Nature Portfolio Reporting Summary linked to this article.

Data availability

All data from shotgun metagenomics analyses in this study have been deposited in the National Center for Biotechnology Information Sequence Read Archive under accession no. PRJNA1242241. Screening of K00169 and K00179 was conducted using KEGG annotations, which are accessible at https://ezmeta.unige.ch/CMMG/functional_annotations/mouse/annotations.tsv. The targeted metabolomics data, including Thermo's raw data files and processed datasets analyzed by Tracefinder 3.2, have been securely stored on an institutional research repository at University of Lausanne. These data are available upon request from the corresponding authors and subject to institutional data-sharing policies. The human study data used in this research are maintained by the Department of Twin Research at King's College London and are not publicly available due to patient privacy and data protection regulations. Researchers seeking access must apply through the established procedures outlined by the Wellcome Trust, following the guidelines provided at <https://twinsuk.ac.uk/researchers/explore-our-data-and-samples/>. Access is granted upon approval and may require specific ethical and governance clearances. All other data and reagents that support the findings of this study are available upon reasonable request from the corresponding authors. Source Data are provided with this paper.

References

1. Bloom, S. I. et al. Mechanisms and consequences of endothelial cell senescence. *Nat. Rev. Cardiol.* **20**, 38–51 (2023).
2. Yrrel, D. J. & Goldstein, D. R. Ageing and atherosclerosis: vascular intrinsic and extrinsic factors and potential role of IL-6. *Nat. Rev. Cardiol.* **18**, 58–68 (2021).
3. Donato, A. J. et al. Mechanisms of dysfunction in the aging vasculature and role in age-related disease. *Circ. Res.* **123**, 825–848 (2018).
4. Han, Y. & Kim, S. Y. Endothelial senescence in vascular diseases: current understanding and future opportunities in senotherapeutics. *Exp. Mol. Med.* **55**, 1–12 (2023).
5. Saeedi Saravi, S. S. & Feinberg, M. W. Can removal of zombie cells revitalize the aging cardiovascular system? *Eur. Heart J.* **45**, 867–869 (2024).
6. Allemann, M.S. et al. Targeting redox system for cardiovascular regeneration in aging. *Aging Cell* **22**, e14020 (2023).
7. Witkowski, M. et al. Gut microbiota and cardiovascular disease. *Circ. Res.* **127**, 553–570 (2020).
8. Fromentin, S. et al. Microbiome and metabolome features of the cardiometabolic disease spectrum. *Nat. Med.* **28**, 303–314 (2022).
9. Chakaroun, R. M. et al. The potential of tailoring the gut microbiome to prevent and treat cardiometabolic disease. *Nat. Rev. Cardiol.* **20**, 217–235 (2023).
10. Zhu, Y. et al. Two distinct gut microbial pathways contribute to meta-organismal production of phenylacetylglutamine with links to cardiovascular disease. *Cell Host. Microbe* **31**, 18–32 (2023).
11. Poesen, R. et al. Microbiota-derived phenylacetylglutamine associates with overall mortality and cardiovascular disease in patients with CKD. *J. Am. Soc. Nephrol.* **27**, 3479–3487 (2016).

12. Romano, K. A. et al. Gut microbiota-generated phenylacetylglutamine and heart failure. *Circ. Heart Fail.* **16**, e009972 (2023).
13. Morita, M. et al. Phenylacetic acid stimulates reactive oxygen species generation and tumor necrosis factor- α secretion in vascular endothelial cells. *Ther. Apher. Dial.* **15**, 147–150 (2011).
14. van der Hee, B. & Wells, J. M. Microbial regulation of host physiology by short-chain fatty acids. *Trends Microbiol.* **29**, 700–712 (2021).
15. Saeedi Saravi, S. S. et al. Dietary omega-3 fatty acid suppresses age-associated thrombotic potential via gut microbiota modulation. *iScience.* **24**, 102897 (2021).
16. Marques, F. Z. et al. High-fiber diet and acetate supplementation change the gut microbiota and prevent the development of hypertension and heart failure in hypertensive mice. *Circulation* **135**, 964–977 (2017).
17. Kalucka, J. et al. Quiescent endothelial cells upregulate fatty acid β -oxidation for vasculoprotection via redox homeostasis. *Cell Metab.* **28**, 881–894 (2018).
18. Nemet, I. et al. A cardiovascular disease-linked gut microbial metabolite acts via adrenergic receptors. *Cell.* **180**, 862–877 (2020).
19. Luo, Y. et al. Predicted visceral adiposity index in relation to risk of coronary heart disease and all-cause mortality: insights from NHANES. *Front. Endocrinol.* **14**, 1296398 (2024).
20. Wiley, C. D. & Campisi, J. The metabolic roots of senescence: mechanisms and opportunities for intervention. *Nat. Metab.* **3**, 1290–1301 (2021).
21. Wu, Y. et al. Phosphoglycerate dehydrogenase activates PKM2 to phosphorylate histone H3T11 and attenuate cellular senescence. *Nat. Commun.* **14**, 1323 (2023).
22. Kabacik, S. et al. The relationship between epigenetic age and the hallmarks of aging in human cells. *Nat. Aging.* **2**, 484–493 (2022).
23. Lee, Y. et al. Histone deacetylase 4 reverses cellular senescence via DDIT4 in dermal fibroblasts. *Aging.* **14**, 4653–4672 (2022).
24. Schader, T. et al. Oxidation of HDAC4 by Nox4-derived H_2O_2 maintains tube formation by endothelial cells. *Redox Biol.* **36**, 101669 (2020).
25. Saeedi Saravi, S. S. et al. Differential endothelial signaling responses elicited by chemogenetic H_2O_2 synthesis. *Redox Biol.* **36**, 101605 (2020).
26. Yang, D. et al. HDAC4 regulates vascular inflammation via activation of autophagy. *Cardiovasc. Res.* **114**, 1016–1028 (2018).
27. Mann, E. R. et al. Short-chain fatty acids: linking diet, the microbiome and immunity. *Nat. Rev. Immunol.* **24**, 577–595 (2024).
28. Das, A. et al. Impairment of an endothelial NAD^+ - H_2S signaling network is a reversible cause of vascular aging. *Cell* **173**, 74–89. e20 (2018).
29. Yang, H. et al. Gut microbial-derived phenylacetylglutamine accelerates host cellular senescence. *Nat. Aging.* **5**, 401–418 (2025).
30. Nemet, I. et al. Atlas of gut microbe-derived products from aromatic amino acids and risk of cardiovascular morbidity and mortality. *Eur. Heart J.* **44**, 3085–3096 (2023).
31. Roos, C. M. et al. Chronic senolytic treatment alleviates established vasomotor dysfunction in aged or atherosclerotic mice. *Aging Cell* **15**, 973–977 (2016).
32. Childs, B. G. et al. Senescent intimal foam cells are deleterious at all stages of atherosclerosis. *Science* **354**, 472–477 (2016).
33. Zhu, Y. et al. The Achilles' heel of senescent cells: from transcriptome to senolytic drugs. *Aging Cell* **14**, 644–658 (2015).
34. Jiang, H. et al. Mechanisms of oxidized LDL-mediated endothelial dysfunction and its consequences for the development of atherosclerosis. *Front. Cardiovasc. Med.* **9**, 925923 (2022).
35. Matsushima, S. et al. Increased oxidative stress in the nucleus caused by Nox4 mediates oxidation of HDAC4 and cardiac hypertrophy. *Circ. Res.* **112**, 651–663 (2013).
36. O'Brien, B. J. et al. CaMKII δ is upregulated by pro-inflammatory cytokine IL-6 in a JAK/STAT3-dependent manner to promote angiogenesis. *FASEB J.* **35**, e21437 (2021).
37. Fukumura, D. et al. Predominant role of endothelial nitric oxide synthase in vascular endothelial growth factor-induced angiogenesis and vascular permeability. *Proc. Natl Acad. Sci. USA.* **98**, 2604–2609 (2001).
38. Chen, X. et al. Therapeutic angiogenesis and tissue revascularization in ischemic vascular disease. *J. Biol. Eng.* **17**, 13 (2023).
39. Lindquist, A. et al. Oral supplementation with the short-chain fatty acid acetate ameliorates age-related aortic stiffening in mice. *Physiology* **38**, S1.5732615 (2023).
40. Poll, B. G. et al. Acetate, a short-chain fatty acid, acutely lowers heart rate and cardiac contractility along with blood pressure. *J. Pharmacol. Exp. Toxicol.* **377**, 39–50 (2021).
41. van Soest, D. M. K. et al. Mitochondrial H_2O_2 release does not directly cause damage to chromosomal DNA. *Nat. Commun.* **15**, 2725 (2024).
42. Adeyemi, D. H. et al. Sodium acetate ameliorates doxorubicin-induced cardiac injury via upregulation of Nrf2/HO-1 signaling and downregulation of NF κ B-mediated apoptotic signaling in Wistar rats. *Naunyn Schmiedeberg's Arch. Pharmacol.* **397**, 423–435 (2024).
43. Kuosmanen, S. M. et al. MicroRNAs mediate the senescence-associated decline of NRF2 in endothelial cells. *Redox Biol.* **18**, 77–83 (2018).
44. Kubben, N. et al. Repression of the antioxidant NRF2 pathway in premature aging. *Cell* **165**, 1361–1374 (2016).
45. Li, J. et al. Targeting the Nrf2 pathway against cardiovascular disease. *Expert Opin. Ther. Targets* **13**, 785–794 (2009).
46. Lewis, K. N. et al. Regulation of Nrf2 signaling and longevity in naturally long-lived rodents. *Proc. Natl Acad. Sci. USA* **112**, 3722–3727 (2015).
47. Sykiotis, G. P. et al. The role of the antioxidant and longevity-promoting Nrf2 pathway in metabolic regulation. *Curr. Opin. Clin. Nutr. Metab. Care* **14**, 41–48 (2011).
48. Ungavri, Z. et al. Resveratrol confers endothelial protection via activation of the antioxidant transcription factor Nrf2. *Am. J. Physiol. Heart Circ. Physiol.* **299**, H18–H24 (2010).
49. Kane, A. E. & Sinclair, D. A. Sirtuins and NAD^+ in the development and treatment of metabolic and cardiovascular diseases. *Circ. Res.* **123**, 868–885 (2018).
50. Martens, C. R. et al. Chronic nicotinamide riboside supplementation is well-tolerated and elevates NAD^+ in healthy middle-aged and older adults. *Nat. Commun.* **9**, 1286 (2018).
51. Thevaranjan, N. et al. Age-associated microbial dysbiosis promotes intestinal permeability, systemic inflammation, and macrophage dysfunction. *Cell Host Microbe* **21**, 455–466 (2017).
52. Kulkarni, A. S. et al. Benefits of metformin in attenuating the hallmarks of aging. *Cell Metab.* **32**, 15–30 (2020).
53. Le Pelletier, L. et al. Metformin alleviates stress-induced cellular senescence of aging human adipose stromal cells and the ensuing adipocyte dysfunction. *eLife* **10**, e62635 (2021).
54. Grootaert, M. O. J. Cell senescence in cardiometabolic diseases. *NPJ Aging* **10**, 46 (2024).
55. Moslehi, J. et al. Telomeres and mitochondria in the aging heart. *Circ. Res.* **110**, 1226–1237 (2012).
56. Xia, L. et al. Resveratrol reduces endothelial progenitor cells senescence through augmentation of telomerase activity by Akt-dependent mechanisms. *Br. J. Pharmacol.* **155**, 387–394 (2008).

57. Csiszar, A. et al. Age-associated proinflammatory secretory phenotype in vascular smooth muscle cells from the non-human primate *Macaca mulatta*: reversal by resveratrol treatment. *J. Gerontol. A Biol. Sci. Med. Sci.* **67**, 811–820 (2012).
58. Wood, D. E. et al. Improved metagenomic analysis with Kraken 2. *Genome Biol.* **20**, 257 (2019).
59. Keiser, S. et al. Comprehensive mouse microbiota genome catalog reveals major difference to its human counterpart. *PLoS Comput. Biol.* **18**, e1009947 (2022).
60. Visconti, A. et al. Interplay between the human gut microbiome and host metabolism. *Nat. Commun.* **10**, 4505 (2019).
61. Blanco-Míguez, A. et al. Extending and improving metagenomic taxonomic profiling with uncharacterized species using MetaPhlan 4. *Nat. Biotechnol.* **41**, 1633–1644 (2023).
62. Shabanian, K. et al. AQP1 differentially orchestrates endothelial cell senescence. *Redox Biol.* **76**, 103317 (2024).
63. Eroglu, E. et al. Discordance between eNOS phosphorylation and activation revealed by multispectral imaging and chemogenetic methods. *Proc. Natl Acad. Sci. USA* **116**, 20210–20217 (2019).
64. Spyropoulos, F. et al. Metabolomic and transcriptomic signatures of chemogenetic heart failure. *Am. J. Physiol. Heart Circ. Physiol.* **322**, H451–H465 (2021).
65. Sorrentino, A. et al. Reversal of heart failure in a chemogenetic model of persistent cardiac redox stress. *Am. J. Physiol. Heart Circ. Physiol.* **317**, H617–H626 (2019).
66. Saeedi Saravi, S. S. et al. Long-term dietary n3 fatty acid prevents aging-related cardiac diastolic and vascular dysfunction. *Vasc. Pharmacol.* **150**, 107175 (2023).

Acknowledgements

We thank T. Michel (Division of Cardiovascular Medicine, Brigham and Women's Hospital, Harvard Medical School) for helpful discussions and technical support (DAAO constructs). We appreciate M. Wannemuehler (Iowa State Univ.) for providing *Clostridium* sp. ASF356. The authors acknowledge funding from the Swiss National Science Foundation grant no. 310030_144152, Stiftung Kardio and Swiss Heart Foundation (to J.H.B.) and from the Swiss National Science Foundation (grant no. CRSK-3_229134), Novartis Foundation for Medical-Biological Research (no. 21A053) and the SwissLife Jubiläumsstiftung (no. 1286) grants (to S.S.S.S.). S.S.S.S. is also funded by the Fonds zur Förderung des Akademischen Nachwuchses (FAN) and Gebauer Stiftung fellowships. K.S. has received support from SwissLife Jubiläumsstiftung (no. 1438) and Wael Almahmeed International Atherosclerosis Society (IAS) Research Fellowship. The Department of Twin Research receives support from grants from the Wellcome Trust (212904/Z/18/Z), the Wellcome Leap Dynamic Resilience program (co-funded by Temasek Trust), the Medical Research Council/British Heart Foundation (MR/M016560/1), European Union, Chronic Disease Research Foundation, Zoe Global, Ltd., the National Institutes of Health and Research Clinical Research Facility and Biomedical Research Centre (based at Guy's and St Thomas' National Health Service Foundation Trust in partnership with King's College London). C.M. is supported by the Chronic Disease Research Foundation (CDRF), the Italian Ministry of Health–Bando Ricerca Corrente 2023 and by the UK Research Innovation/Medical Research Council (MR/W026813/1 and MR/Y010175). I.A. is funded by an Amsterdam Cardiovascular Sciences post-doctoral grant (2022–2023).

Author contributions

S.S.S.S. and J.H.B. conceptualized and designed the study. S.S.S.S. drafted, wrote and revised the manuscript. S.S.S.S., K.S., T.S., M.S., G.K., M.A. and P.L. performed the experiments, including mouse studies, in vivo mono-colonization, fecal DNA extraction, senescence and signal transduction studies, senolytic therapy, immunofluorescence assays, angiogenesis assays and vasorelaxation studies. F.C. and B.P. performed shotgun metagenomic data analysis, in vitro bacterial studies and acetate quantification. A.T. and S.L. performed LC–MS/MS quantification of the levels of PAA and PAGln in plasma and culture medium. C.M., I.A., X.Z., A.V. and M.F. analyzed and provided data from the human TwinsUK cohort. M.C. and A.A. conducted analysis of senescence biomarkers. All authors provided intellectual contributions and approved the final manuscript. S.S.S.S., F.R., F.P. and J.H.B. obtained funding. S.S.S.S. directed and supervised all aspects of the study.

Funding

Open access funding provided by University of Zurich.

Competing interests

The authors declare no competing interests.

Additional information

Extended data is available for this paper at <https://doi.org/10.1038/s43587-025-00864-8>.

Supplementary information The online version contains supplementary material available at <https://doi.org/10.1038/s43587-025-00864-8>.

Correspondence and requests for materials should be addressed to Seyed Soheil Saeedi Saravi or Jürg H. Beer.

Peer review information *Nature Aging* thanks Tohru Minamino and the other, anonymous, reviewer(s) for their contribution to the peer review of this work.

Reprints and permissions information is available at www.nature.com/reprints.

Publisher's note Springer Nature remains neutral with regard to jurisdictional claims in published maps and institutional affiliations.

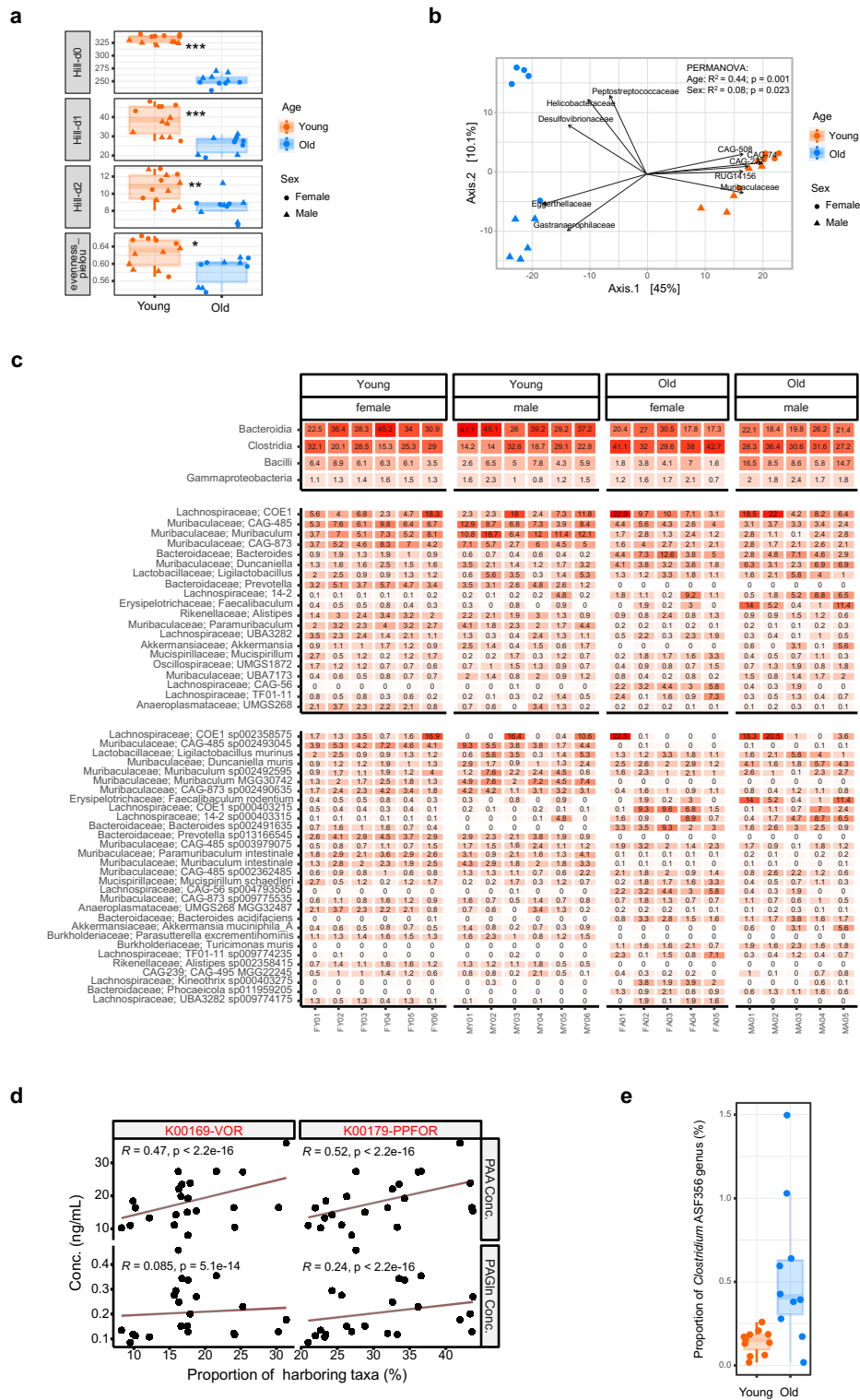
Open Access This article is licensed under a Creative Commons Attribution 4.0 International License, which permits use, sharing, adaptation, distribution and reproduction in any medium or format, as long as you give appropriate credit to the original author(s) and the source, provide a link to the Creative Commons licence, and indicate if changes were made. The images or other third party material in this article are included in the article's Creative Commons licence, unless indicated otherwise in a credit line to the material. If material is not included in the article's Creative Commons licence and your intended use is not permitted by statutory regulation or exceeds the permitted use, you will need to obtain permission directly from the copyright holder. To view a copy of this licence, visit <http://creativecommons.org/licenses/by/4.0/>.

© The Author(s) 2025

¹Center for Translational and Experimental Cardiology, Department of Cardiology, University Hospital Zurich, University of Zurich, Schlieren, Switzerland.

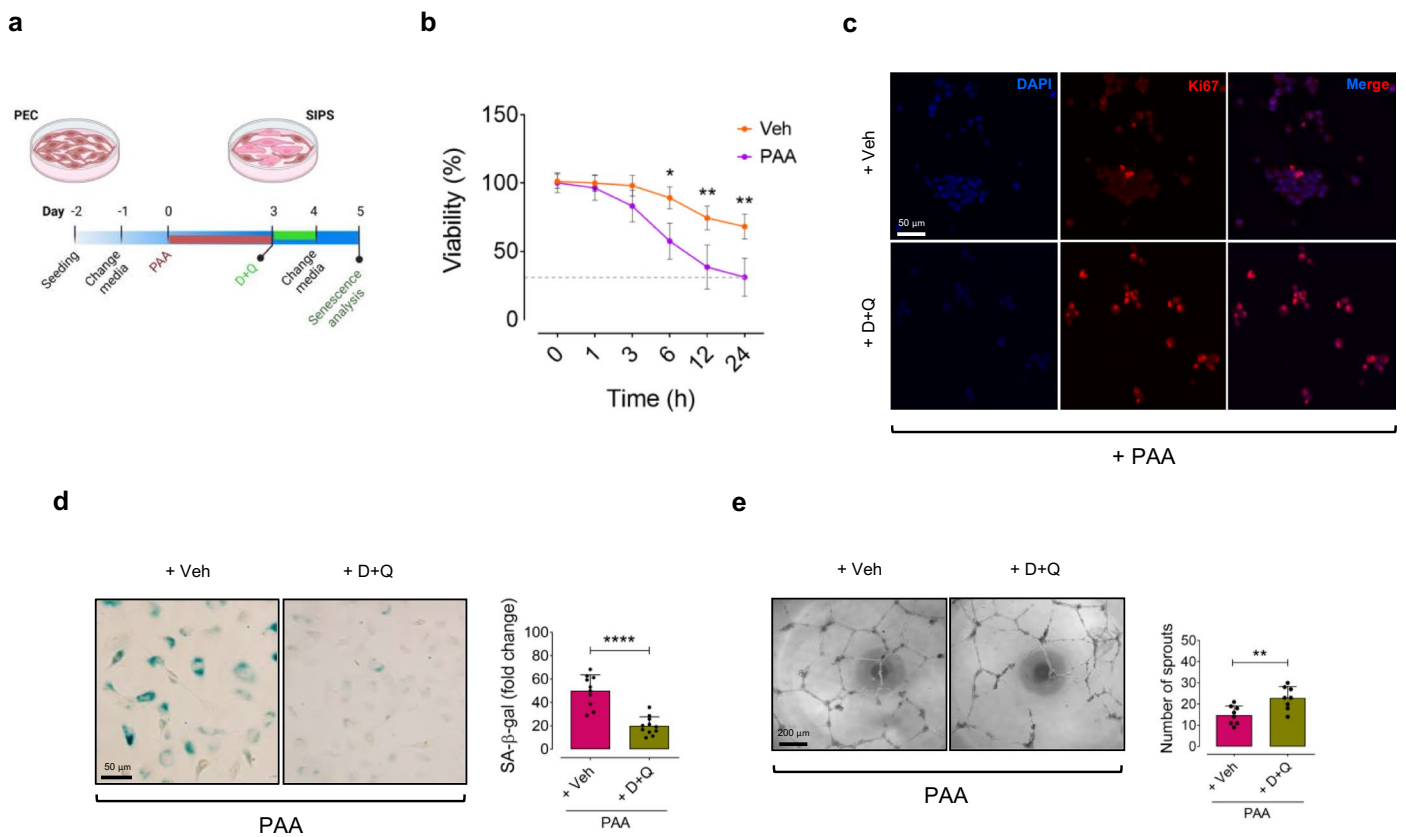
²University Heart Center, Department of Cardiology, University Hospital Zurich, Zurich, Switzerland. ³Laboratory of Food Biotechnology, Institute of Food, Nutrition and Health, Department of Health Sciences and Technology, ETH Zurich, Zurich, Switzerland. ⁴Department for Gastroenterology and Hepatology, University Hospital Zurich, University of Zurich, Zurich, Switzerland. ⁵Faculty Unit of Toxicology, University Center of Legal Medicine, Lausanne University Hospital and University of Lausanne, Lausanne, Switzerland. ⁶Unit of Forensic Toxicology and Chemistry, University Center of Legal

Medicine, Lausanne University Hospital and University of Lausanne, Geneva University Hospital and University of Geneva, Lausanne, Geneva, Switzerland. ⁷Institute of Clinical Chemistry, University Hospital Zurich, Schlieren, Switzerland. ⁸Institute of Oncology Research (IOR), Bellinzona, Switzerland. ⁹Università della Svizzera Italiana, Lugano, Switzerland. ¹⁰Department of Twin Research, King's College London, St Thomas' Hospital Campus, London, UK. ¹¹Department of Pathophysiology and Transplantation, Università Degli Studi di Milano, Milan, Italy. ¹²Fondazione IRCCS Cà Granda Ospedale Maggiore Policlinico, Angelo Bianchi Bonomi Hemophilia and Thrombosis Center, Milan, Italy. ¹³Amsterdam Cardiovascular Sciences, Diabetes & Metabolism, Amsterdam, Netherlands. ¹⁴Center for Molecular Cardiology, University of Zurich, Schlieren, Switzerland. ¹⁵Department of Internal Medicine, Cantonal Hospital Baden, Baden, Switzerland. ¹⁶Centre for Biostatistics, Epidemiology, and Public Health, Department of Clinical and Biological Sciences, University of Turin, Turin, Italy. ¹⁷Department of Medicine, University of Padova, Padova, Italy. ¹⁸Department of Health Sciences and Technology (D-HEST), ETH Zurich, Zurich, Switzerland. ¹⁹Oncology Institute of Southern Switzerland, Ente Ospedaliero Cantonale, Bellinzona, Switzerland. ²⁰These authors contributed equally: Seyed Soheil Saeedi Saravi, Jürg H. Beer. ✉e-mail: soheil.saeedi@uzh.ch; hansjuerg.beer@ksb.ch



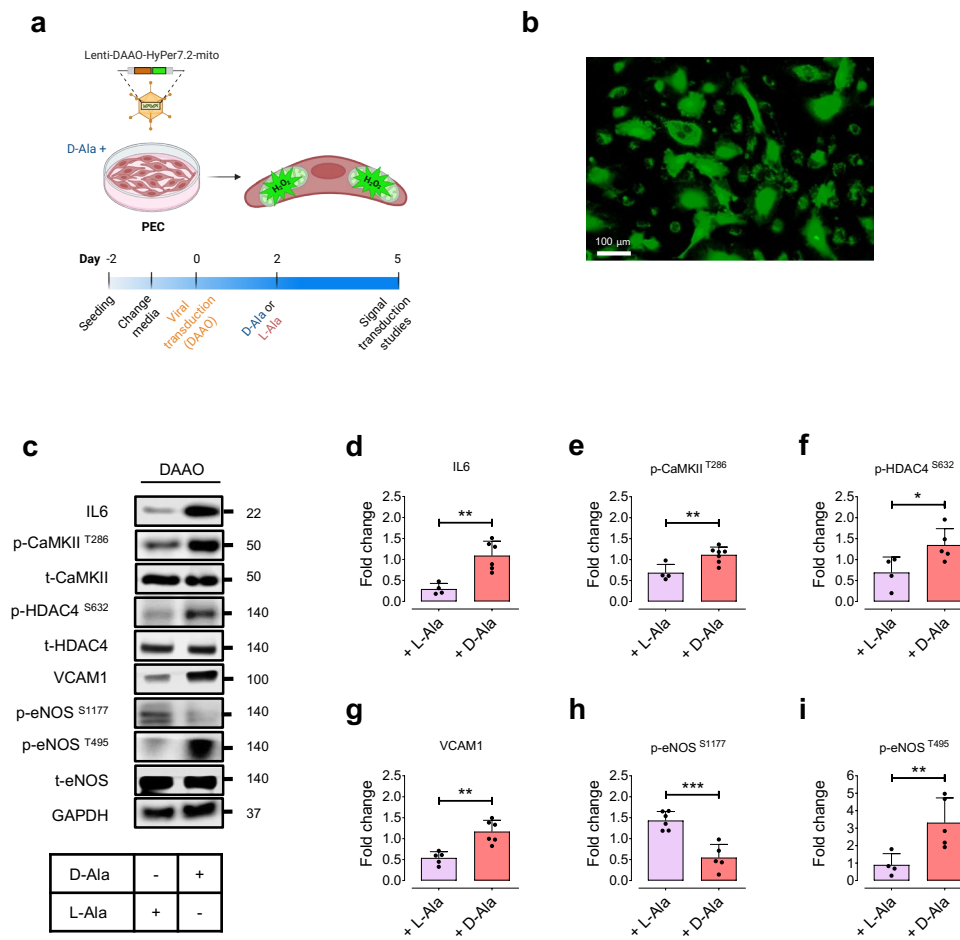
Extended Data Fig. 1 | Age-associated gut microbiota alterations. **a**, Box plots representing alpha diversity in feces of female and male, old and young C57BL/6J mice measured by Hill-d0 to 2 and Pielou's evenness indices ($n = 5-6$). **b**, Principal coordinate analysis (PCoA) plot showing beta diversity based on the community level changes in old and young mice ($n = 5-6$). **c**, Heatmap depicting differentially abundant microbial profiles at the strain level (each color represents one bacterial taxa) in the fecal microbiota of female and male, old versus young mice ($n = 5-6$). **d**, Gene-metabolite interactions explain a positive correlation of the proportion (%) of either VOR- or PPFOR-harboring taxa and plasma PAA levels in aged mice. Nevertheless, the lowermost chart shows non-significant association

of VOR or PPFOR homologs and plasma PAGin levels in these mice ($n = 5-6$). **e**, Distribution of the *Clostridium* genus in mouse microbiomes. The box plots show the higher proportion (%) of taxa belonging to the *Clostridium* genus in the microbiome of aged mice compared to young mice ($n = 5-6$). Error bars represent SEM (**a, b, d, e**). Data were analyzed using Kruskal-Wallis statistical test (**a**), Atchinson distance and permutational multivariate analysis of variance (PERMANOVA) (**b**), partial Spearman's correlation test tests (**d**), and two-tailed unpaired Student's *t*-test (**e**). (* $P < 0.05$, ** $P < 0.01$, *** $P < 0.001$). Source data are provided as a Source Data file.



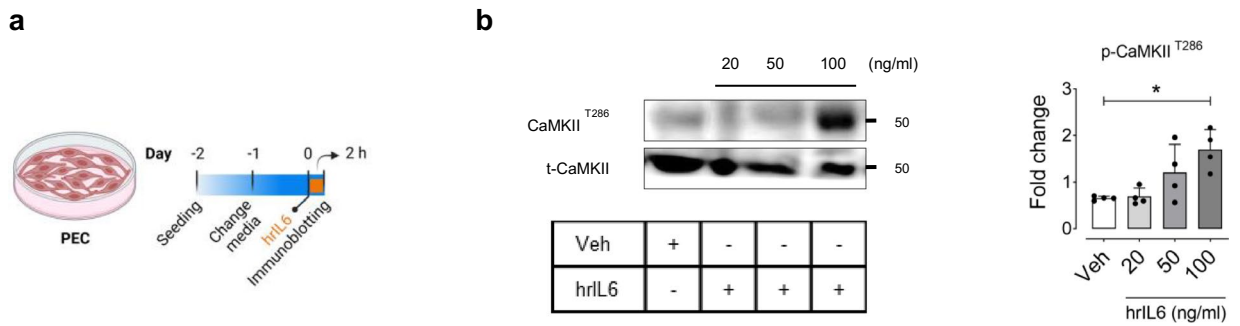
Extended Data Fig. 2 | D + Q reduces senescence in PAA-exposed ECs. a, Schematic diagram of the experimental setting: PECs were treated with PAA (10 μ M, for 72 h) in the presence or absence of Dasatinib+Quercetin (D + Q: 500 nM + 20 μ M, for 24 h), followed by assessment of senescence phenotype and tube formation. **b,** Cell counts demonstrate that D + Q significantly reduces the viability percentage (%) of PAA-exposed PECs over Veh-treated PECs. The cells at passages 3 to 5 were characterized as PEC (n = 6). **c,d,** D + Q ameliorates PAA-induced senescence phenotype in HAECs: (c) Ki67 immunostaining shows that D + Q markedly increases the number of Ki67⁺ PECs (n = 6);

(d) Representative images of SA- β -gal staining demonstrates that D + Q significantly decreases the number of SA- β -gal⁺ cells (%) (n = 6). **e,** Confocal images represent the 2D matrigel tube formation of PAA-exposed PECs treated with D + Q or vehicle. Right, quantitative plot shows a significantly higher number of tubes formed by D + Q-treated PECs compared to vehicle counterparts (n = 8). Scale bar, 50 and 200 μ m. Experiments were triplicated independently. Statistical analysis was performed with a one-way ANOVA followed by Tukey's post *hoc* test (b) and a two-tailed unpaired Student's *t*-test (c, d). Images created with [BioRender.com](https://www.biorender.com) (a). (* P < 0.05, ** P < 0.01, **** P < 0.0001).



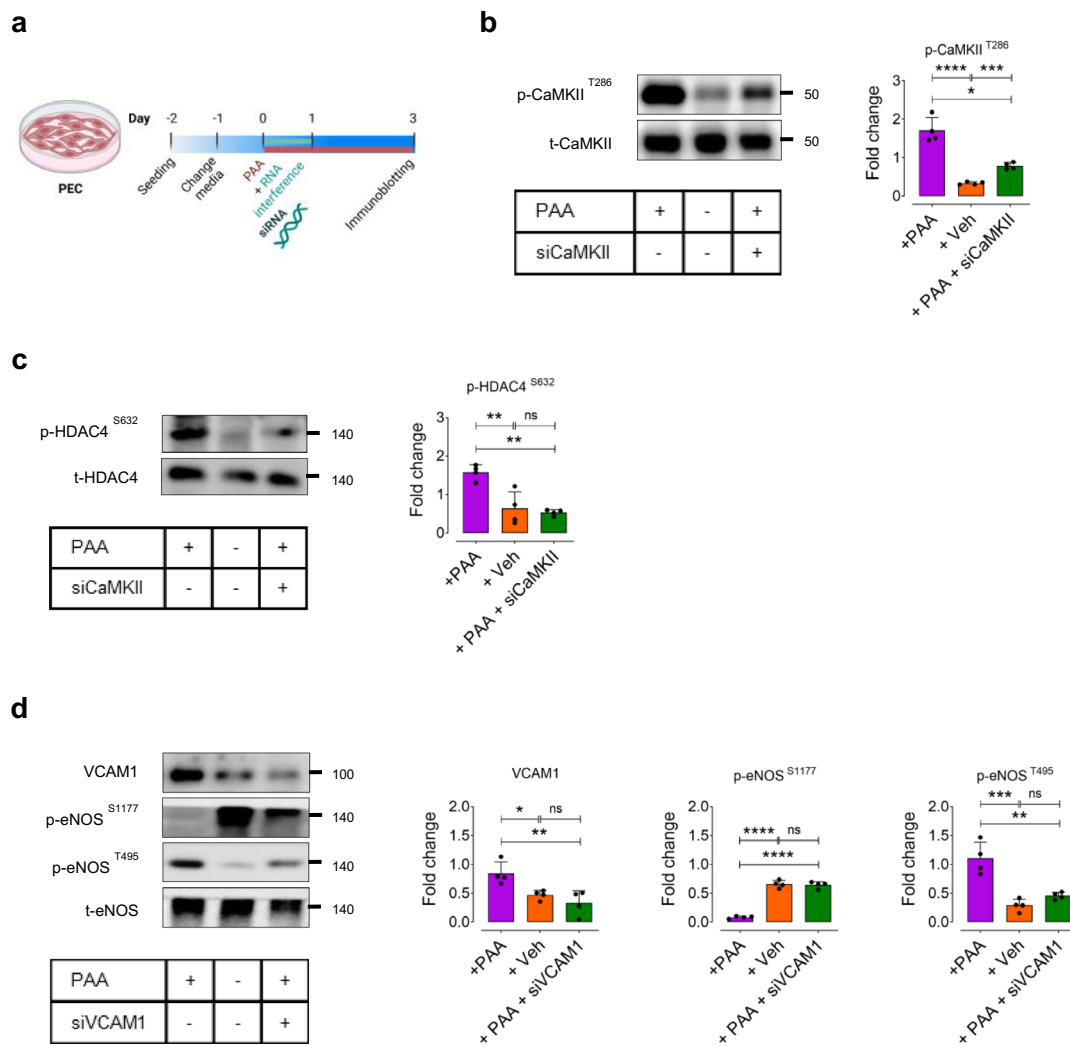
Extended Data Fig. 3 | Chemogenetic mitochondrial H_2O_2 regulates endothelial NO signaling through IL-6-HDAC4 pathway. a, Schematic diagram of the experimental setting: PECs were transduced with lentiviral vectors encoding D-amino acid oxidase (DAAO)-HyPer7.2 targeted to the cell mitochondria for generation of mitochondrial H_2O_2 in the presence of D-alanine (10 mM) for 72 h. **b**, Representative widefield ratiometric HyPer7.2 images of PECs transduced with Lenti-DAAO-HyPer7.2-mito constructs. **c-i**, Immunoblots (c)

and quantitative plots show that chemogenetic mitochondrial H_2O_2 , produced by DAAO in response to D-alanine but not L-alanine, orchestrates IL-6-mediated CaMKII-HDAC4 phosphorylation and the subsequent VCAM1-regulated eNOS phosphorylation at Ser1177 and Thr495 in PECs ($n = 4-6$). Scale bar, 100 μm . Error bars represent SD (**d-i**). Data represent triplicated biologically independent experiments. P values were calculated using a two-tailed unpaired Student's t -test (**d-i**). Images created with [BioRender.com](https://www.biorender.com) (a). (* $P < 0.05$, ** $P < 0.01$, *** $P < 0.001$).



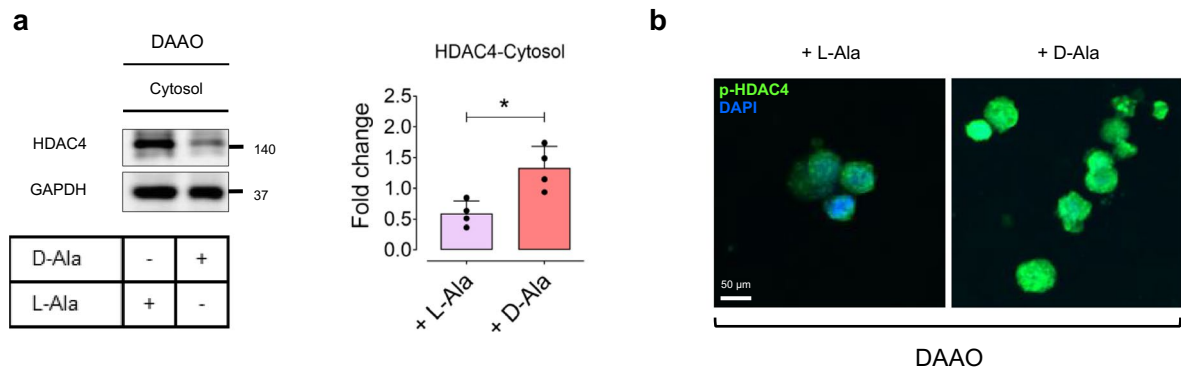
Extended Data Fig. 4 | hrIL6 regulates CaMKII post-translation modification in ECs. a, Schematic diagram of the experimental setting: PECs were treated with the human recombinant IL-6 (hrIL6) at specific concentrations (0, 20, 50, 100 ng/ml) for 2 h. **b**, Immunoblots (Left) and quantitative plots (Right) demonstrate that hrIL6 dose-dependently increases CaMKII phosphorylation at Thr286 in PECs

(n = 6). Error bars represent SD (**b**). Experiments were triplicated independently. *P* values were calculated using one-way ANOVA followed by Tukey's post *hoc* test (**b**). Images created with [BioRender.com](https://www.biorender.com) (**a**). (***) *P* < 0.001). Source data are provided as a Source Data file.



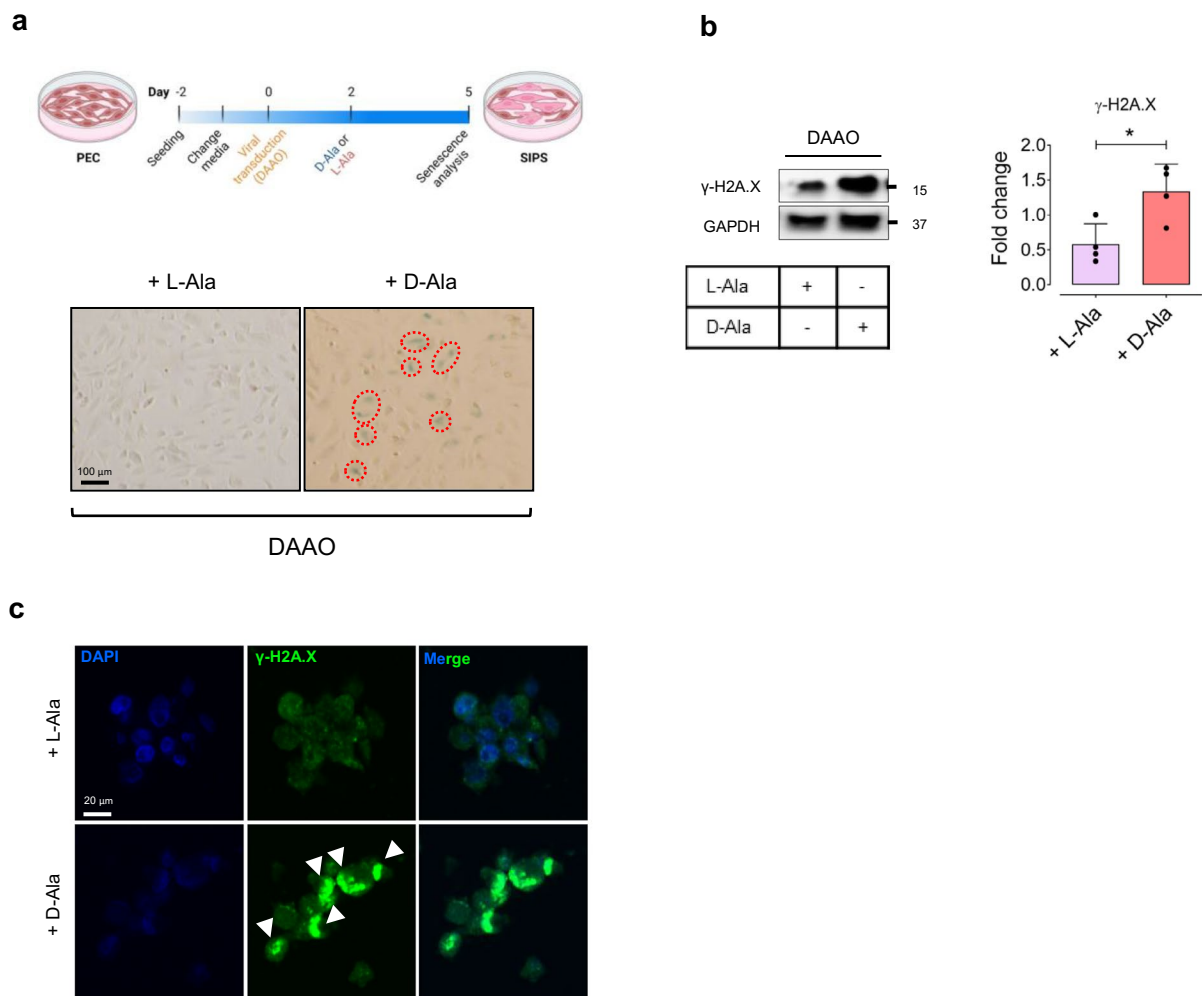
Extended Data Fig. 5 | CaMKII-mediated SASP pathway underlies PAA-induced EC dysfunction. **a**, Schematic diagram of the experimental setting: PECs were transfected with siCaMKII or siVCAM1 (for 24 h) in the presence or absence of PAA (10 μ M, for 72 h). **b**, **c**, Immunoblots (left) and quantitative plots (right) characterizing the effects of PAA on the PAA-induced post-translational modifications of CaMKII (**b**) and its downstream epigenetic regulator HDAC4 (**c**) using CaMKII knockdown approach in PECs (n = 4). **d**, Analysis of VCAM1

expression and eNOS phosphorylation at Ser1177 and Thr495 in siVCAM1-transfected PECs in the presence or absence of PAA (n = 4). Error bars represent SD (**b-d**). Data represent triplicated biologically independent experiments. P values were calculated using one-way ANOVA followed by Tukey's post hoc test (**b-d**). Images created with [BioRender.com](https://www.biorender.com) (**a**). (* $P < 0.05$, ** $P < 0.01$, *** $P < 0.001$, **** $P < 0.0001$, ns, not significant). Source data are provided as a Source Data file.



Extended Data Fig. 6 | H₂O₂ orchestrates HDAC4 phosphorylation and its nuclear export. **a**, Immunoblots (Left) and quantitative plot (Right) reveal HDAC4 nuclear export, represented as an increased expression in the cytosol in response to intracellular H₂O₂ generated by DAAO in the presence of D-alanine (10 mM, for 72 h) in PECs (n = 4). **b**, p-HDAC4 immunostaining shows that

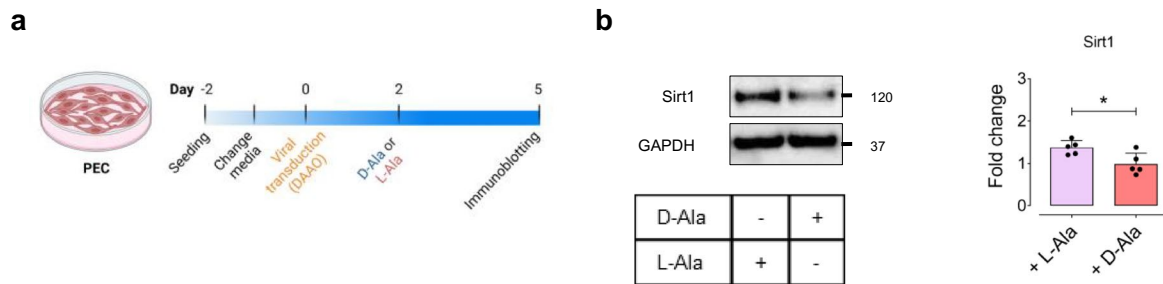
intracellular H₂O₂ markedly increases HDAC4 phosphorylation that facilitates its translocation towards the cell cytosol in PECs (n = 6). Scale bar, 50 μ m. Error bars represent SD (**a**). Data represent triplicated biologically independent experiments. *P* values were calculated using a two-tailed unpaired Student's *t*-test (**a**). (**P* < 0.05). Source data are provided as a Source Data file.



Extended Data Fig. 7 | Chemogenetic H_2O_2 promotes EC senescence.

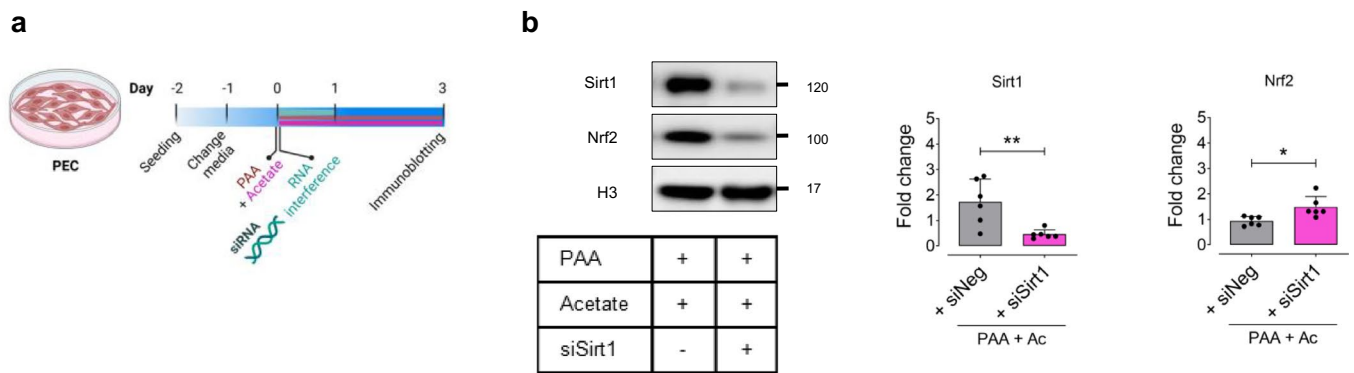
a, Schematic diagram of the experimental setting: PECs were transduced with lentiviral vectors encoding D-amino acid oxidase (DAAO) targeted to the cell mitochondria for generation of mitochondrial H_2O_2 in the presence D-alanine (10 mM) for 72 h. Representative images of SA- β -gal staining demonstrates that DAAO-mediated mitochondrial H_2O_2 induced cellular senescence in PECs, as shown by increased SA- β -gal-positive cells (%) ($n = 6$). **b**, **c**, Immunoblots (**b**) and

γ -H2A.X immunostaining images (**c**) reveal a marked increase in DDR following mitochondrial H_2O_2 production in DAAO-transduced PECs incubated with D-alanine ($n = 4-6$). Scale bar, 20 and 100 μ m. Red circles indicate SA- β -gal-positive cells. Error bars represent SD (**b**). Data represent triplicated biologically independent experiments. P values were calculated using a two-tailed unpaired Student's t -test (**b**). Images created with [BioRender.com](https://www.biorender.com) (**a**). ($*P < 0.05$). Source data are provided as a Source Data file.



Extended Data Fig. 8 | Mitochondrial H₂O₂ suppresses Sirt1 in ECs. **a**, Schematic diagram of the experimental setting: PECs were transduced with lentiviral vector encoding DAAO-mito, followed by treatment with D-alanine (10 mM) for 72 h for generation of H₂O₂ in cell mitochondria. **b**, Immunoblots (Left) and quantitative plots (Right) demonstrate that mitochondrial H₂O₂ significantly reduces

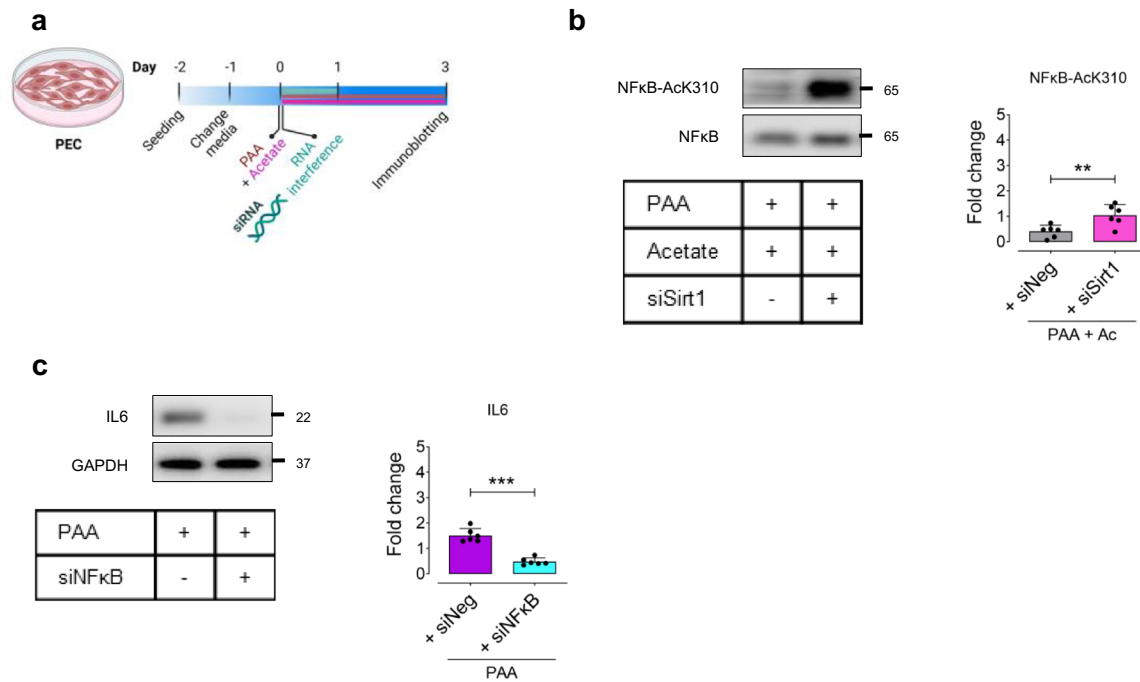
Sirt1 expression in PECs (n = 5–6). Error bars represent SD (**b**). Data represent triplicated biologically independent experiments. *P* values were calculated using a two-tailed unpaired Student's *t*-test (**b**). Images created with [BioRender.com](https://www.biorender.com) (**a**). (**P* < 0.05). Source data are provided as a Source Data file.



Extended Data Fig. 9 | Acetate regulates Nrf2 by Sirt1 modulation in ECs.

a, Schematic diagram of the experimental setting: PECs were transfected with siNeg or siSirt1 (for 24 h) in the presence of PAA plus sodium acetate (10 μ M + 3 μ M, for 72 h). **b**, Immunoblots (Left) and quantitative plots (Right) show that silencing of Sirt1 (by siSirt1) significantly reduces the expression of Sirt1 and Nrf2 (deacetylated form) in the nuclei of PECs treated with PAA

plus sodium acetate compared to those transfected with siNeg (n = 6). Error bars represent SD (**b**). Data represent triplicated biologically independent experiments. *P* values were calculated using a two-tailed unpaired Student's *t*-test (**b**). Images created with [BioRender.com](https://www.biorender.com) (**a**). (**P* < 0.05, ***P* < 0.01). Source data are provided as a Source Data file.



Extended Data Fig. 10 | Acetate-mediated SASP downregulation is dependent on Sirt1 in ECs. **a**, Schematic diagram of the experimental setting: PECs were transfected with siNeg, siSirt1, or siNFκB (for 24 h) in the presence of PAA plus sodium acetate (10 μM + 3 μM, for 72 h) or PAA alone (10 μM, for 72 h). **b**, Immunoblots (top) and quantitative plots (bottom) demonstrate that Sirt1 knockdown markedly increases NFκB acetylation at Lys310 in PECs incubated with PAA plus sodium acetate compared to siNeg-transfected counterparts

(n = 6). **c**, Immunoblots show that the SASP component IL-6 is downregulated in siNFκB-transfected PECs in the presence of PAA (n = 6). Error bars represent SD (**b,c**). Data represent triplicated biologically independent experiments. *P* values were calculated using a two-tailed unpaired Student's *t*-test (**b,c**). Images created with [BioRender.com](https://www.biorender.com) (**a**). (***P* < 0.01, ****P* < 0.001). Source data are provided as a Source Data file.

Reporting Summary

Nature Portfolio wishes to improve the reproducibility of the work that we publish. This form provides structure for consistency and transparency in reporting. For further information on Nature Portfolio policies, see our [Editorial Policies](#) and the [Editorial Policy Checklist](#).

Statistics

For all statistical analyses, confirm that the following items are present in the figure legend, table legend, main text, or Methods section.

n/a Confirmed

- The exact sample size (n) for each experimental group/condition, given as a discrete number and unit of measurement
- A statement on whether measurements were taken from distinct samples or whether the same sample was measured repeatedly
- The statistical test(s) used AND whether they are one- or two-sided
Only common tests should be described solely by name; describe more complex techniques in the Methods section.
- A description of all covariates tested
- A description of any assumptions or corrections, such as tests of normality and adjustment for multiple comparisons
- A full description of the statistical parameters including central tendency (e.g. means) or other basic estimates (e.g. regression coefficient) AND variation (e.g. standard deviation) or associated estimates of uncertainty (e.g. confidence intervals)
- For null hypothesis testing, the test statistic (e.g. F , t , r) with confidence intervals, effect sizes, degrees of freedom and P value noted
Give P values as exact values whenever suitable.
- For Bayesian analysis, information on the choice of priors and Markov chain Monte Carlo settings
- For hierarchical and complex designs, identification of the appropriate level for tests and full reporting of outcomes
- Estimates of effect sizes (e.g. Cohen's d , Pearson's r), indicating how they were calculated

Our web collection on [statistics for biologists](#) contains articles on many of the points above.

Software and code

Policy information about [availability of computer code](#)

Data collection
CellRox green imaging: LAS X Office 1.4.6.28433 (Leica);
Opal fluorescence imaging: Phenochart 1.2.0 (Akoya Biosciences);
HyPer7.2 Fluorescence Imaging: Metafluor Software (Molecular Devices);
Ex vivo vasorelaxation assay: LabChart v7.2.5 (AD Instruments, Inc.)

Data analysis
Metabolites Identification: Tracefinder 3.2 (Thermo Scientific);
Metagenomic Analysis: Trimmomatic v0.39, https://ftp.ncbi.nlm.nih.gov/genomes/all/GCF/000/001/635/GCF_000001635.27_GRCm39/
GCF_000001635.27_GRCm39_genomic.fna.gz;
Taxonomic Profiling: kraken2/Bracken2 (<https://ezmeta.unige.ch/CMMG/Kraken2db/cmmg>), MetaPhlAn v.4.0 & Bowtie 2 v.2.3.4.3 pipelines;
KEGG Functional annotations: https://ezmeta.unige.ch/CMMG/functional_annotations/mouse/annotations.tsv;
Vegan v2.5-5 package (<https://github.com/vegan>);
Fecal Acetate Level Analysis: EZChrom A.04.10 (Agilent);
GraphPad Prism 9 (v.9.5.1, La Jolla, CA, USA);
R v1.26.1 (Vienna, Austria, 2017);
R package 'lmerTest' (v3.1.3, function 'lmer');
ImageJ software 1.54j (Fiji).

For manuscripts utilizing custom algorithms or software that are central to the research but not yet described in published literature, software must be made available to editors and reviewers. We strongly encourage code deposition in a community repository (e.g. GitHub). See the Nature Portfolio [guidelines for submitting code & software](#) for further information.

Data

Policy information about [availability of data](#)

All manuscripts must include a [data availability statement](#). This statement should provide the following information, where applicable:

- Accession codes, unique identifiers, or web links for publicly available datasets
- A description of any restrictions on data availability
- For clinical datasets or third party data, please ensure that the statement adheres to our [policy](#)

We declare that Source Data and Supplementary Information are provided with this paper. All data from shotgun metagenomics analyses in this study have been deposited in the National Center for Biotechnology Information Sequence Read Archive (SRA) under accession number PRJNA1242241. Screening of K00169 and K00179 was conducted using KEGG annotations, which are accessible at https://ezmeta.unige.ch/CMMG/functional_annotations/mouse/annotations.tsv. The targeted metabolomics data, including Thermo's raw data files and processed datasets analyzed by Tracefinder 3.2, have been securely stored on an institutional research repository at University of Lausanne. These data are available upon request from the corresponding authors and subject to institutional data-sharing policies. The human study data used in this research are maintained by the Department of Twin Research at King's College London and are not publicly available due to patient privacy and data protection regulations. Researchers seeking access must apply through the established procedures outlined by the Wellcome Trust, following the guidelines provided at <https://twinsuk.ac.uk/resources-for-researchers/access-our-data/>. Access is granted upon approval and may require specific ethical and governance clearances. All other data and reagents that support the findings of this study are available upon reasonable request from the corresponding authors.

Research involving human participants, their data, or biological material

Policy information about studies with [human participants or human data](#). See also policy information about [sex, gender \(identity/presentation\), and sexual orientation](#) and [race, ethnicity and racism](#).

| | |
|--|---|
| Reporting on sex and gender | The human analyses were performed on both female and male subjects. |
| Reporting on race, ethnicity, or other socially relevant groupings | The reports are provided by the the Department of Twin Research at King's College London. |
| Population characteristics | The TwinsUK cohort includes more than 14,000 adult twins of the same sex between 18 and 95 years old. All participants received no compensation and provided written informed consent. |
| Recruitment | Data were collected by the TwinsUK biobank. Participants were recruited from the general UK population through national media campaigns. Other than the subjects being mostly females, no selection biases can be expected to impact results. |
| Ethics oversight | The study was approved by the NRES Committee London-Westminster (REC Reference No.: EC04/015). All participants in TwinsUK Cohort received no compensation and provided written informed consent. |

Note that full information on the approval of the study protocol must also be provided in the manuscript.

Field-specific reporting

Please select the one below that is the best fit for your research. If you are not sure, read the appropriate sections before making your selection.

Life sciences Behavioural & social sciences Ecological, evolutionary & environmental sciences

For a reference copy of the document with all sections, see nature.com/documents/nr-reporting-summary-flat.pdf

Life sciences study design

All studies must disclose on these points even when the disclosure is negative.

| | |
|-----------------|--|
| Sample size | No statistical methods were used to pre-determine sample sizes, but similar sample sizes were used in previous publications (Saeedi Saravi, S.S. et al., 2023, 2021; Shabaniyan, K. et al., 2024). In TwinsUK human study, participants that exhibited values below the detection level (0) for PAA or PAGIn were considered as not available. Accordingly, PAA and PAGIn were measured in plasma samples of 7,303 subjects by Metabolon using a non-targeted UPLC-MS/MS platform. |
| Data exclusions | No animals or data points were excluded from experiments or analyses. |
| Replication | All attempts at replication were successful. At least three independent triplicated experiments were performed for each experimental set-up. |
| Randomization | No method of randomization was used to assign animals to experimental groups. |
| Blinding | The investigators in this study were blinded to the conditions of the experiments, except for oral gavage (for Clos, PAA, or D+Q administration) to avoid cross-contamination within the groups. |

Reporting for specific materials, systems and methods

We require information from authors about some types of materials, experimental systems and methods used in many studies. Here, indicate whether each material, system or method listed is relevant to your study. If you are not sure if a list item applies to your research, read the appropriate section before selecting a response.

Materials & experimental systems

| n/a | Involved in the study |
|-------------------------------------|---|
| <input type="checkbox"/> | <input checked="" type="checkbox"/> Antibodies |
| <input type="checkbox"/> | <input checked="" type="checkbox"/> Eukaryotic cell lines |
| <input checked="" type="checkbox"/> | <input type="checkbox"/> Palaeontology and archaeology |
| <input type="checkbox"/> | <input checked="" type="checkbox"/> Animals and other organisms |
| <input checked="" type="checkbox"/> | <input type="checkbox"/> Clinical data |
| <input checked="" type="checkbox"/> | <input type="checkbox"/> Dual use research of concern |
| <input checked="" type="checkbox"/> | <input type="checkbox"/> Plants |

Methods

| n/a | Involved in the study |
|-------------------------------------|---|
| <input checked="" type="checkbox"/> | <input type="checkbox"/> ChIP-seq |
| <input checked="" type="checkbox"/> | <input type="checkbox"/> Flow cytometry |
| <input checked="" type="checkbox"/> | <input type="checkbox"/> MRI-based neuroimaging |

Antibodies

Antibodies used

anti-phospho-CaMKII Thr286 (1:1000; CST, 12716)
 anti-total-CaMKII (1: 1000; CST, 4436)
 anti-phospho-HDAC4 Ser632 (1:1000; CST, 3424)
 anti-total-HDAC4 (1:1000; CST, 7628)
 anti-H3 (1:1000; CST, 9715)
 anti-phospho-eNOS Ser1177 (1:1000; CST, 9517)
 anti-phospho-eNOS Thr495 (1:1000; CST, 9574)
 anti-total-eNOS (1: 1000; CST, 32027)
 anti-phospho-Histone H2A.X Ser139 (1:1000; CST, 80312)
 anti-Acetyl-NF-κB p65 (Lys310) (1:1000; CST, 3045)
 anti-total-NF-κB p65 (1:1000; CST, 8242)
 anti-ACSS2 (1:1000; CST, 3658)
 anti-IDH2 (1:1000; CST, 56439)
 anti-Sirt1 (1:1000; CST, 9475)
 anti-Nrf2 (1:1000; CST, 12721)
 anti-Col3a1 (1:1000; CST, 30565)
 anti-MMP-9 (1:1000; CST, 3852)
 anti-VCAM-1 (1:1000; Invitrogen, MA5-31965)
 anti-IL6 (1:1000; Invitrogen, M-620)
 anti-NADPH oxidase 4 (NOX4) (1:1000; Invitrogen, PA5-72816)
 anti-hTERT (1:500; Invitrogen, MA5-16034)
 anti-VE Cadherin (1:100; Invitrogen, PA5-19612)
 anti-CD31 (1:100; eBioscience, 14-0311-82)
 anti-Histone H3ac (Pan-Acetyl) (1:500; Santa Cruz Biotechnology, sc-518011)
 anti-phospho-HDAC4 Ser632 (1:100; abcam, ab39408-1001)
 anti-p16INK4a (1:100 and 1:1000; abcam, ab211542),
 conjugated secondary anti-Alexa Fluor® 488 (1:2000; abcam, ab150157)
 conjugated secondary anti-Alexa Fluor® 594 (1:2000; abcam, ab150080)
 conjugated secondary anti-Alexa Fluor® 647 (1:2000; abcam, ab150075)
 anti-goat anti-rabbit IgG-HRP (1:2000; Southern Biotechnology, 4030-05)
 anti-goat anti-mouse IgG-HRP (1:2000; Southern Biotechnology, 1036-05)

Validation

According to the data sheet, all the antibodies used for immunoblotting, immunofluorescence staining, and Opal Multiplex immunofluorescence can detect target proteins. Also, Alexa Fluor antibodies are suitable for tissue immunostaining according to the data sheet. All primary and secondary antibodies were validated for the application (see citations provided on manufacturers websites for the above outlined catalogue numbers).

Eukaryotic cell lines

Policy information about [cell lines and Sex and Gender in Research](#)

Cell line source(s)

Primary human aortic endothelial cells (HAEC; Lonza, CC-2535)

Authentication

Primary human aortic endothelial cells (HAEC; Lonza, CC-2535)

Mycoplasma contamination

Cultured cells were regularly tested for mycoplasma contamination. We have confirmed the negative results for the cells used in our experiments.

Animals and other research organisms

Policy information about [studies involving animals](#); [ARRIVE guidelines](#) recommended for reporting animal research, and [Sex and Gender in Research](#)

| | |
|-------------------------|---|
| Laboratory animals | We have reported necessary information appropriately in the manuscript. 8 week old wild-type C57BL/6J mice were obtained from the Jackson Laboratory and maintained in our facility for specific times for normal aging modeling. All mice were individually housed in controlled environments in plexiglass cages under a strict 12 h:12 h light/dark cycles at an ambient temperature of $23 \pm 1^\circ\text{C}$ and humidity of $55 \pm 10\%$, and fed standard chow diet (Research Diets) until 3 (as Young) or >24 (as Old) months of age. Mice had access to drinking water and food ad libitum. 10-12-week-old wild-type C57BL/6J mice were obtained from the Jackson Laboratory and maintained in our facility for in vivo bacterial colonization. |
| Wild animals | There was no wild animal used in the study. |
| Reporting on sex | Equal numbers of both female and male mice were used. |
| Field-collected samples | There were no field-collected samples used in the study. |
| Ethics oversight | Our research complies with all ethical regulations approved by the Institutional Animal Care and Use Committee at University of Zurich and the Cantonal Ethics Commission Zurich (ZH023/2023 and ZH241/19). |

Note that full information on the approval of the study protocol must also be provided in the manuscript.

Plants

| | |
|-----------------------|--|
| Seed stocks | <i>Report on the source of all seed stocks or other plant material used. If applicable, state the seed stock centre and catalogue number. If plant specimens were collected from the field, describe the collection location, date and sampling procedures.</i> |
| Novel plant genotypes | <i>Describe the methods by which all novel plant genotypes were produced. This includes those generated by transgenic approaches, gene editing, chemical/radiation-based mutagenesis and hybridization. For transgenic lines, describe the transformation method, the number of independent lines analyzed and the generation upon which experiments were performed. For gene-edited lines, describe the editor used, the endogenous sequence targeted for editing, the targeting guide RNA sequence (if applicable) and how the editor was applied.</i> |
| Authentication | <i>Describe any authentication procedures for each seed stock used or novel genotype generated. Describe any experiments used to assess the effect of a mutation and, where applicable, how potential secondary effects (e.g. second site T-DNA insertions, mosaicism, off-target gene editing) were examined.</i> |